

EMPRESS. II. HIGHLY Fe-ENRICHED METAL-POOR GALAXIES WITH ~ 1.0 (Fe/O)_⊙ AND 0.02 (O/H)_⊙ : POSSIBLE TRACES OF SUPER MASSIVE ($> 300M_{\odot}$) STARS IN EARLY GALAXIES

TAKASHI KOJIMA^{1,2}, MASAMI OUCHI^{3,1,4}, MICHAEL RAUCH⁵, YOSHIKI ONO¹, KIMHIKO NAKAJIMA³, YUKI ISOBE^{1,2},
SEIJI FUJIMOTO^{6,7}, YUICHI HARIKANE^{3,8,1}, TAKUYA HASHIMOTO⁹, MASAO HAYASHI³, YUTAKA KOMIYAMA³,
HARUKA KUSAKABE¹⁰, JI HOON KIM^{11,12}, CHIEN-HSIU LEE¹³, SHIRO MUKAE^{1,14}, TOHRU NAGAO¹⁵,
MASATO ONODERA^{11,16}, TAKATOSHI SHIBUYA¹⁷, YUMA SUGAHARA^{18,3,1,2}, MASAYUKI UMEMURA¹⁹, KIYOTO YABE⁴

Draft version June 9, 2020

ABSTRACT

We present element abundance ratios and ionizing radiation of local young low-mass ($\sim 10^6 M_{\odot}$) extremely metal poor galaxies (EMPGs) with a 2% solar oxygen abundance (O/H)_⊙ and a high specific star-formation rate (sSFR $\sim 300 \text{ Gyr}^{-1}$), and other (extremely) metal poor galaxies, which are compiled from Extremely Metal-Poor Representatives Explored by the Subaru Survey (EMPRESS) and the literature. Weak emission lines such as [Fe III]4658 and He II4686 are detected in very deep optical spectra of the EMPGs taken with 8m-class telescopes including Keck and Subaru (Kojima et al. 2019; Izotov et al. 2018), enabling us to derive element abundance ratios with photoionization models. We find that neon- and argon-to-oxygen ratios are comparable to those of known local dwarf galaxies, and that the nitrogen-to-oxygen abundance ratios (N/O) are lower than 20% (N/O)_⊙ consistent with the low oxygen abundance. However, the iron-to-oxygen abundance ratios (Fe/O) of the EMPGs are generally high; the EMPGs with the 2%-solar oxygen abundance show high Fe/O ratios of $\sim 90 - 140\%$ (Fe/O)_⊙, which are unlikely explained by suggested scenarios of Type Ia supernova iron productions, iron's dust depletion, and metal-poor gas inflow onto previously metal-riched galaxies with solar abundances. Moreover, these EMPGs have very high He II4686/H β ratios of $\sim 1/40$, which are not reproduced by existing models of high-mass X-ray binaries whose progenitor stellar masses are less than $120 M_{\odot}$. Comparing stellar-nucleosynthesis and photoionization models with a comprehensive sample of EMPGs identified by this and previous EMPG studies, we propose that both the high Fe/O ratios and the high He II4686/H β ratios are explained by the past existence of super massive ($> 300 M_{\odot}$) stars, which may evolve into intermediate-mass black holes ($\gtrsim 100 M_{\odot}$).

Subject headings: galaxies: dwarf — galaxies: evolution — galaxies: formation — galaxies: abundance — galaxies: ISM

E-mail: tkojima@icrr.u-tokyo.ac.jp

¹ Institute for Cosmic Ray Research, The University of Tokyo, 5-1-5 Kashiwanoha, Kashiwa, Chiba 277-8582, Japan

² Department of Physics, Graduate School of Science, The University of Tokyo, 7-3-1 Hongo, Bunkyo, Tokyo 113-0033, Japan

³ National Astronomical Observatory of Japan, 2-21-1 Osawa, Mitaka, Tokyo 181-8588, Japan

⁴ Kavli Institute for the Physics and Mathematics of the Universe (WPI), University of Tokyo, Kashiwa, Chiba 277-8583, Japan

⁵ Carnegie Observatories, 813 Santa Barbara Street, Pasadena, CA 91101, USA

⁶ Cosmic Dawn Center (DAWN), Copenhagen, Denmark

⁷ Niels Bohr Institute, University of Copenhagen, Lyngbyvej 2, DK2100 Copenhagen, Denmark

⁸ Department of Physics and Astronomy, University College London, Gower Street, London WC1E 6BT, UK

⁹ Tomonaga Center for the History of the Universe (TCHoU), Faculty of Pure and Applied Sciences, University of Tsukuba, Tsukuba, Ibaraki 305-8571, Japan

¹⁰ Observatoire de Genève, Université de Genève, 51 Ch. des Maillettes, 1290 Versoix, Switzerland

¹¹ Subaru Telescope, National Astronomical Observatory of Japan, National Institutes of Natural Sciences (NINS), 650 North Aohoku Place, Hilo, HI 96720, USA

¹² Metaspaces, 36 Nonhyeon-ro, Gangnam-gu, Seoul 06312, Republic of Korea

¹³ NSF's National Optical Infrared Astronomy Research Laboratory, Tucson, AZ 85719, USA

¹⁴ Department of Astronomy, Graduate School of Science, The University of Tokyo, 7-3-1 Hongo, Bunkyo, Tokyo, 113-

0033, Japan

¹⁵ Research Center for Space and Cosmic Evolution, Ehime University, 2-5 Bunkyo-cho, Matsuyama, Ehime 790-8577, Japan

¹⁶ Department of Astronomical Science, SOKENDAI (The Graduate University for Advanced Studies), Osawa 2-21-1, Mitaka, Tokyo, 181-8588, Japan

¹⁷ Kitami Institute of Technology, 165 Koen-cho, Kitami, Hokkaido 090-8507, Japan

¹⁸ Waseda Research Institute for Science and Engineering, Faculty of Science and Engineering, Waseda University, 3-4-1, Okubo, Shinjuku, Tokyo 169-8555, Japan

¹⁹ Center for Computational Sciences, University of Tsukuba, Tsukuba, Ibaraki 305-8577, Japan.

[†] Partly based on data obtained with the Subaru Telescope. The Subaru Telescope is operated by the National Astronomical Observatory of Japan.

[‡] The data presented herein were partly obtained at the W. M. Keck Observatory, which is operated as a scientific partnership among the California Institute of Technology, the University of California and the National Aeronautics and Space Administration. The Observatory was made possible by the generous financial support of the W. M. Keck Foundation.

[#] This paper includes data gathered with the 6.5 meter Magellan Telescopes located at Las Campanas Observatory, Chile.

1. INTRODUCTION

The early universe is dominated by a large number of young, low-mass, metal-poor galaxies. Theoretical arguments suggest that the first galaxies are formed at $z \sim 10$ –20 from gas already metal-enriched by Pop-III (i.e., metal free) stars. According to hydrodynamical simulations (e.g., Wise et al. 2012), the first galaxies are created in dark matter (DM) mini halos with $\sim 10^8 M_\odot$ and have low stellar masses ($\log(M_*/M_\odot) \sim 4$ –6), low metallicities ($Z \sim 0.1$ –1% Z_\odot), and high specific star-formation rates ($\text{sSFR} \sim 100 \text{ Gyr}^{-1}$) at $z \sim 10$. The typical stellar mass is remarkably small, comparable to those of star clusters. Such cluster-like galaxies are undergoing an early stage of the galaxy formation. One of critical goals of the modern cosmology is to understand the early-stage galaxy formation by probing the cluster-like, star-forming galaxies (SFGs).

The stellar population and the star-formation history are critical information to understand galaxies undergoing the early-phase star formation. Element abundances such as iron (Fe) and nitrogen (N) are good tracers of the past star formation and the stellar population because these elements are produced and ejected by the different stellar populations at different ages. First, iron elements are effectively produced and released into ISM by type-Ia supernovae (SNe) ~ 1 Gyr after the start of the star formation. The type-Ia SNe are triggered by gas accretion from a main sequence star onto a white dwarf, whose progenitor weighs ~ 1 –10 M_\odot (e.g., Nomoto et al. 2013), in a binary system. The type-Ia SNe start contributing to the increase of iron-to-oxygen ratio (Fe/O) at the age of ~ 1 Gyr (e.g., Steidel et al. 2016). As reported in studies of Galactic stars (Bensby & Feltzing 2006; Lecureur et al. 2007; Bensby et al. 2013), the increasing Fe/O trend is seen in a metallicity range of $Z_*/Z_\odot \gtrsim 0.2$ (corresponding to $12+\log(\text{O}/\text{H}) \gtrsim 8.0$). Below $12+\log(\text{O}/\text{H}) \sim 8.0$ (or $\lesssim 1$ Gyr), the core-collapse SNe mainly contribute to the production and release of iron and oxygen. Under the assumption of this mechanism, low-mass, metal-poor, young SFGs are expected to have a low Fe/O ratio due to their young ages. Second, nitrogen elements trace activities of massive stars and low- and intermediate-mass stars at low and high metallicities, respectively. As suggested by previous studies (Pérez-Montero & Contini 2009; Pérez-Montero et al. 2013; Andrews & Martini 2013), nitrogen-to-oxygen ratios (N/O) of SFGs present a plateau in the range of $12+\log(\text{O}/\text{H}) \lesssim 8.0$ and a positive slope at higher metallicities as a function of metallicity. Model calculations of the N/O evolution (e.g., Vincenzo et al. 2016) also support this trend. The plateau basically results from the primary nucleosynthesis of massive stars, while the positive slope is mainly attributed to the secondary nucleosynthesis of low- and intermediate-mass stars (e.g., Vincenzo et al. 2016). In the nitrogen-enrichment mechanism, low-mass, metal-poor, young SFGs may have a low N/O ratio because of their low metallicities and young ages.

Ionizing radiation is another key to understand the stellar population of galaxies in the early-phase star formation. Ionizing radiation is produced by massive stars and/or a hot accretion disk around compact objects such as black holes (BHs). Observational studies

(López-Sánchez & Esteban 2010; Shirazi & Brinchmann 2012; Senchyna et al. 2017; Schaerer et al. 2019) have suggested that SFGs show strong He II4686 emission lines represented by $\text{He II4686}/\text{H}\beta \sim 1/300$ –1/30. Especially, the $\text{He II4686}/\text{H}\beta$ shows an increasing trend as metallicity decreases in the range of $12+\log(\text{O}/\text{H}) < 8.0$. The He II4686 line is sensitive to ionizing photons above 54.4 eV, which are not abundant in radiation of O- and B-type hot stars. Under the assumption of stellar radiation, Xiao et al. (2018) have created nebular emission models with the combination of the photoionization code CLOUDY (Ferland et al. 2013) and the BPASS (Binary Population and Spectral Synthesis) code (Stanway et al. 2016; Eldridge et al. 2017). The Xiao et al. (2018) models predict $\text{He II4686}/\text{H}\beta \lesssim 1/1000$, well below the observed $\text{He II4686}/\text{H}\beta$ ratios of $\sim 1/300$ to $\sim 1/30$ (Schaerer et al. 2019). This means that the main contributors of He II4686 are not hot stars. Schaerer et al. (2019) have estimated $\text{He II4686}/\text{H}\beta$ ratios with high mass X-ray binary (HMXB) models of Fragos et al. (2013a,b), and suggested that high $\text{He II4686}/\text{H}\beta$ ratios can be partly explained by the HMXB models. However, the HMXB models still do not explain the high $\text{He II4686}/\text{H}\beta$ ratios for galaxies with a high H β equivalent width, $\text{EW}_0(\text{H}\beta) > 100 \text{ \AA}$ (i.e., younger than 5 Myr). Schaerer et al. (2019) suggest another possible contribution from old stellar population and/or shock-heated gas. The main contributor of the He II4686 emission is still under debate.

In the local universe, extremely metal-poor galaxies (EMPGs) have been discovered (e.g., Izotov & Thuan 1998; Thuan et al. 2005; Izotov et al. 2009, 2018, 2019; Ly et al. 2014) by exploiting wide-field data such as Sloan Digital Sky Survey (SDSS, York et al. 2000). These galaxies have low metallicities, $12+\log(\text{O}/\text{H}) \sim 7.0$ –7.2, low stellar masses, $\log(M_*/M_\odot) \sim 6$ –8, and high sSFR, $\sim 100 \text{ Gyr}^{-1}$. Such local EMPGs are regarded as local analogs of high- z galaxies because they have low metallicities, low stellar masses, and large emission line equivalent widths similar to low-mass galaxies with $\log(M_*/M_\odot) \sim 6$ –8 at $z \sim 2$ –3 (Christensen et al. 2012a,b; Stark et al. 2014; Vanzella et al. 2017) and $z \sim 6$ –7 (Stark et al. 2015; Mainali et al. 2017). However, the stellar mass ranges of the previous studies, $\log(M_*/M_\odot) \sim 6$ –8, are not as low as cluster-like galaxies in the early-stage of the galaxy formation, $\log(M_*/M_\odot) \sim 4$ –6, as described above. To reach a lower mass range than the previous EMPG studies (e.g., SDSS, i -band limiting magnitude ~ 21 mag), deeper, wide-field imaging survey has been expected.

We have initiated a new EMPG survey with wide-field optical imaging data obtained in Subaru/Hyper Suprime-Cam (HSC; Miyazaki et al. 2012, 2018; Komiyama et al. 2018; Kawanomoto et al. 2018; Furusawa et al. 2018) Subaru Strategic Program (HSC-SSP; Aihara et al. 2018) in Kojima et al. (2019, Paper I hereafter). The new EMPG survey has been named “Extremely Metal-Poor Representatives Explored by the Subaru Survey” (EMPRESS). We have created a source sample based on the deep, wide-field HSC-SSP data, which covers $\sim 500 \text{ deg}^2$ area with a 5σ limit of ~ 26 mag in Paper I.

This paper is the second paper from our EMPRESS

project. The detailed sample selection and results of the first spectroscopic observations have been reported in Paper I. These paper will be followed by other papers in which we investigate details of size and morphology, and kinematics of our EMPG sample (e.g., Isobe et al. 2020, Paper III hereafter). The outline of this paper is as follows. In Section 2, we briefly explain our samples selected from the Subaru HSC-SSP data and the SDSS data. In Section 3, we describe our optical spectroscopy carried out for our EMPG candidates and explain the reduction and calibration processes of our spectroscopy data. In Section 4, we measure emission line fluxes and estimate galaxy properties such as stellar mass, star-formation rate, metallicity, and element abundance. Section 5 shows results and discussions of element abundance ratios and ionizing radiation. Then Section 6 summarizes this paper. Throughout this paper, magnitudes are on the AB system (Oke & Gunn 1983). We adopt the following cosmological parameters, $(h, \Omega_m, \Omega_\Lambda) = (0.7, 0.3, 0.7)$. The definition of the solar metallicity is given by $12+\log(\text{O}/\text{H})=8.69$ (Asplund et al. 2009). We also define an EMPG as a galaxy with $12+\log(\text{O}/\text{H}) < 7.69$ (i.e., $Z/Z_\odot < 0.1$) in this paper, which is almost the same as in previous metal-poor galaxy studies (e.g., Kunth & Östlin 2000; Izotov et al. 2012; Guseva et al. 2017).

2. SAMPLE

This paper uses samples obtained by Paper I. In Paper I, we select the EMPG candidates from HSC-SSP and SDSS data with our machine learning (ML) classifier. We briefly describe selections of EMPG candidates in this section. Hereafter, these candidates chosen from the HSC-SSP and SDSS source catalogs are called “HSC-EMPG candidates” and “SDSS-EMPG candidates”, respectively.

2.1. HSC-EMPG candidates

We use the HSC-SSP internal data of the S17A and S18A data releases, which are explained in the second data release (DR2) paper of HSC-SSP (Aihara et al. 2019). Although the HSC-SSP survey data are taken in three layers of Wide, Deep, and UltraDeep, we only use the Wide field layer in this study. In the HSC-SSP S17A and S18A data releases, images were reduced with the HSC pipeline, `hscPipe` v5.4 and v6.7 (Bosch et al. 2018), respectively, with codes of the Large Synoptic Survey Telescope (LSST) software pipeline (Ivezić et al. 2019a; Axelrod et al. 2010; Jurić et al. 2015; Ivezić et al. 2019b). The pipeline conducts the bias subtraction, flat fielding, image stacking, astrometry and zero-point magnitude calibration, source detection, and magnitude measurement. As reported in Paper I, there are slight differences in our results between S17A and S18A data due to the different pipeline versions. Thus, although part of the S17A and S18A data are duplicated, we use both S17A and S18A data in this study to maximize the size of our EMPG sample. The details of the observations, data reduction, detection, photometric catalog, and pipeline are described in Aihara et al. (2019) and Bosch et al. (2018). We use `cmodel` magnitudes (Bosch et al. 2018) corrected for Milky-Way dust extinction (Schlegel et al. 1998) in the estimation of the total magnitudes of a source.

Below we explain how we construct an HSC source catalog, from which we select EMPG candidates. We use isolated or cleanly deblended sources that fall within *griz*-band images. We also require that none of the pixels in their footprints are interpolated, none of the central 3×3 pixels are saturated, none of the central 3×3 pixels suffer from cosmic rays, and there are no bad pixels in their footprints. Then we exclude sources whose `cmodel` magnitude or centroid position measurements have a problem. We require a detection in the *griz*-band images. We mask sources close to a bright star (Coupon et al. 2018; Aihara et al. 2019) in the S18A data. Here we select objects whose photometric measurements are brighter than 5σ limiting magnitudes, $g < 26.5$, $r < 26.0$, $i < 25.8$, and $z < 25.2$ mag, which are estimated by Ono et al. (2018) with 1.5-arcsec diameter circular apertures. We also require that the photometric measurement errors are less than 0.1 mag in *griz* bands. Finally, we obtain 17,912,612 and 40,407,765 sources in total from the HSC-SSP S17A and S18A data, respectively, with the selection criteria explained above. The effective area is 205.82 and 508.84 deg² in the HSC-SSP S17A and S18A data, respectively. See Paper I for details of our HSC source sample.

We select EMPG candidates from the HSC-SSP source catalog in four steps: i) An initial rough selection based on colors, extendedness, and blending. ii) the ML classifier selection. iii) Transient object removal by measuring the flux variance in multi-epoch images. iv) Visual inspection of the *gri*-composite images. Refer to Paper I for the selection details. Eventually, we obtain 12 and 21 HSC-EMPG candidates from the S17A and S18A catalogs, respectively. We find that 6 out of the HSC-EMPG candidates are duplicated between the S17A and S18A catalogs. Thus the number of our independent HSC-EMPG candidates is 27 (=12+21−6). A magnitude range of the 27 HSC-EMPG candidates is $i = 19.3\text{--}24.3$ mag.

2.2. SDSS-EMPG candidates

We construct a SDSS source catalog from the 13th release (DR13; Albareti et al. 2017) of the SDSS photometry data. Although the SDSS data are ~ 5 mag shallower ($i_{\text{lim}} \sim 21$ mag) than HSC-SSP data ($i_{\text{lim}} \sim 26$ mag), we also select EMPG candidates from the SDSS data to complement brighter EMPGs. Here we select objects whose photometric measurements are brighter than SDSS limiting magnitudes, $u < 22.0$, $g < 22.2$, $r < 22.2$, $i < 21.3$, and $z < 21.3$ mag²³. We only obtain objects whose magnitude measurement errors are < 0.1 mag in *ugriz* bands. Note that we use `Modelmag` for the SDSS data. Among flags in the `PhotoObjALL` catalog, we require that a `clean` flag is “1” (i.e., *True*) to remove objects with photometry measurement issues. The `clean` flag²⁴ eliminates the duplication, deblending/interpolation problems, suspicious detections, and detections at the edge of an image. We also remove objects with a *True* cosmic-ray flag and/or a *True* blended flag, which often mimics a broad-band excess in photom-

²³ Magnitudes reaching 95% completeness, which are listed in <https://www.sdss.org/dr13/scope/>

²⁴ Details are described in http://www.sdss.org/dr13/algorithms/photo_flags_recommend/

etry. We reject relatively large objects with a ninety-percent petrosian radius greater than 10 arcsec to eliminate contamination by HII regions in nearby spiral galaxies. Finally, we derive 31,658,307 sources in total from the SDSS DR13 photometry data. The total unique area of SDSS DR13 data is 14,555 deg².

We select EMPG candidates from the SDSS source catalog similarly to the HSC source catalog in Section 2.1. After the selection, we derive 86 SDSS-EMPG candidates from the SDSS source catalog, whose *i*-band magnitudes range $i = 14.8\text{--}20.9$ mag. One out of the 86 candidates (HSC J1429–0110) is also selected as an HSC-EMPG candidate in Section 2.1. Details are described in Paper I.

3. SPECTROSCOPIC DATA

In this section, we explain our spectroscopic data of 10 galaxies described in Paper I, which are selected from our HSC and SDSS source catalogs and confirmed to be metal-poor galaxies. We have identified that the 2 out of the 10 metal-poor galaxies (HSC J1631+4426 and SDSS J2115–1734) satisfy the EMPG condition of $Z < 0.10Z_{\odot}$ with metallicity estimates based on the electron temperature measurement. HSC J1631+4426 shows a metallicity of $0.016 Z_{\odot}$, which is the lowest metallicity reported to date. In addition to the 10 metal-poor galaxies, we include another EMPG from the literature (J0811+4730, Izotov et al. 2018) in the sample of this paper. J0811+4730 has the second lowest metallicity of $0.019 Z_{\odot}$ reported to date.

In paper I, we report on our spectroscopy of the 10 metal-poor galaxies performed with 4 spectrographs of the Low Dispersion Survey Spectrograph 3 (LDSS-3) and the Magellan Echellette Spectrograph (MagE) on Magellan telescope, the Deep Imaging Multi-Object Spectrograph (DEIMOS) on Keck-II telescope, and the Faint Object Camera And Spectrograph (FOCAS) on Subaru telescope. Although the spectroscopy and reduction are detailed in Paper I, we briefly summarize them in Sections 3.1–3.4. In Section 3.5, we newly report very faint emission lines detected in our spectroscopy, such as [O III]4363, [Ar IV]4711, [Fe III]4658, He II4686, [N II]6584, and [Ar III]7136, which are required to estimate element abundance ratios and constrain the FUV spectral hardness (Section 1).

3.1. Magellan/LDSS-3

We conducted spectroscopy for one galaxy selected from our HSC catalog (HSC J1429–0110) with LDSS-3 at Magellan telescope. We used the VPH-ALL grism with the $0''.75 \times 4'$ long-slit, which was placed at the offset position two-arcmin away from the center of the long-slit mask so that the spectroscopy could cover the bluer side. The exposure time was 3,600 seconds. The spectroscopy covered $\lambda \sim 3,700\text{--}9,500$ Å with a spectral resolution of $R \equiv \lambda/\Delta\lambda \sim 860$.

We used the IRAF package to reduce and calibrate the LDSS-3 data. The reduction and calibration processes include the bias subtraction, flat fielding, one-dimensional (1D) spectrum subtraction, sky subtraction, wavelength calibration, flux calibration, and atmospheric-absorption correction. A one-dimensional spectrum was derived from an aperture centered on

the blue compact component of our galaxies. A standard star, CD-32 9972 was used in the flux calibration. The wavelengths were calibrated with the HeNeAr lamp. Atmospheric absorption was corrected with the extinction curve at Cerro Tololo Inter-American Observatory (CTIO). Our LDSS-3 spectroscopy may have been affected by the atmospheric refraction because a slit was not necessarily placed perpendicular to the horizon (i.e., at a parallactic angle) in our spectroscopy, which may lead to the wavelength-dependent slit loss. The slit angles of each target are determined so that we can simultaneously observe multiple emission regions. To estimate the wavelength-dependent slit loss $SL(\lambda)$ carefully, we made a model of the atmospheric refraction.

3.2. Magellan/MagE

We carried out spectroscopy for 8 galaxies selected from our HSC and SDSS catalogs (HSC J2314+0154, HSC J1142–0038, SDSS J0002+1715, SDSS J1642+2233, SDSS J2115–1734, SDSS J2253+1116, SDSS J2310–0211, and SDSS J2253+1116) with MagE of Magellan telescope. We used the echellette grating with the $0''.85 \times 10''$ or $1''.2 \times 10''$ longslits. The exposure time was 1,800 or 3,600 seconds, depending on luminosities of the galaxies. The MagE spectroscopy covered $\lambda \sim 3,100\text{--}10,000$ Å with a spectral resolution of $R \equiv \lambda/\Delta\lambda \sim 4,000$.

To reduce the raw data taken with MagE, we used the MagE pipeline from Carnegie Observatories Software Repository²⁵. The MagE pipeline has been developed on the basis of the *Carpy* package (Kelson et al. 2000; Kelson 2003). The bias subtraction, flat fielding, scattered light subtraction, two-dimensional (2D) spectrum subtraction, sky subtraction, wavelength calibration, cosmic-ray removal, 1D-spectrum subtraction were conducted with the MagE pipeline. Details of these pipeline processes are described on the web site of Carnegie Observatories Software Repository mentioned above. One-dimensional spectra were subtracted by summing pixels along the slit-length direction on a 2D spectrum.

We conducted the flux calibration with the standard star, Feige 110, using IRAF routines. Wavelengths were calibrated with emission lines of the ThAr lamp. Spectra of each order were calibrated separately and combined with the weight of electron counts to generate a single 1D spectrum. Atmospheric absorption was corrected in the same way as in Section 3.1. Our MagE spectroscopy may have been also affected by the atmospheric refraction for the same reason as the LDSS-3 spectroscopy. Thus, we corrected the wavelength-dependent slit loss carefully in the same manner as the LDSS-3 spectroscopy described in Section 3.1.

3.3. Keck/DEIMOS

We conducted spectroscopy for one galaxy selected from our HSC catalog (HSC J1631+4426) with DEIMOS of the Keck-II telescope. We used the multi-object mode with the $0''.8$ slit width. The exposure time was 2,400 seconds. We used the 600ZD grating and the BAL12 filter with a blaze wavelength at 5,500 Å. The DEIMOS

²⁵ <https://code.obs.carnegiescience.edu>

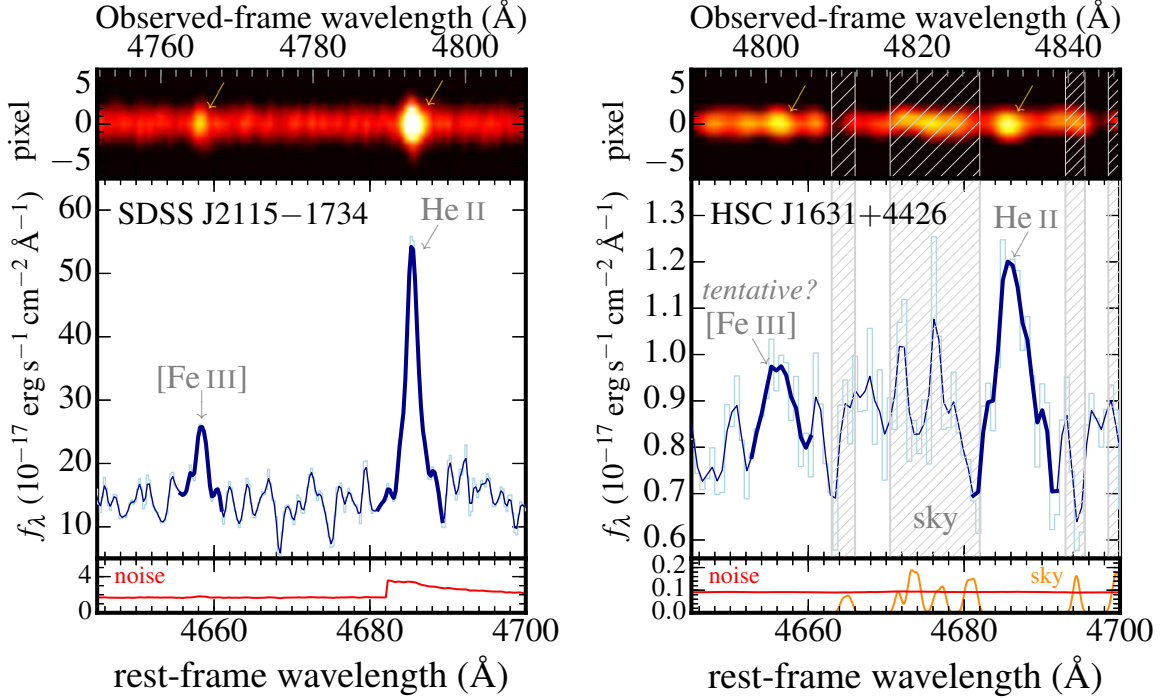


FIG. 1.— Spectra of SDSS J2115–1734 (left) and HSC J1631+4426 (right) taken in our MagE and FOCAS spectroscopy, respectively, around the [Fe III]4658 and He II4686 emission lines. The top, center, and bottom panels show 2D spectra, signal spectra, and noise+sky spectra, respectively. In the center panel, the light blue line is the un-smoothed background subtracted spectrum, while the dark blue line is spectra smoothed with a Gaussian profile. The shaded regions indicate positions of the sky emission lines. In the bottom panel, we exhibit a noise spectrum with the red lines. The orange line show a sky emission spectrum (in arbitrary units) modeled with the sky emission data of Hanuschik (2003). For SDSS J2115–1734, no sky emission line falls on the wavelength range of this panel.

spectroscopy covered $\lambda \sim 3,800\text{--}8,000$ Å with a spectral resolution of $R \equiv \lambda/\Delta\lambda \sim 1,500$.

We used the IRAF package to reduce and calibrate the DEIMOS data. The reduction and calibration processes were the same as the LDSS-3 data explained in Section 3.1. A standard star, G191B2B was used in the flux calibration. Wavelengths were calibrated with the NeAr-KrXe lamp. Atmospheric absorption was corrected under the assumption of the extinction curve at Mauna Kea Observatories. We only used a spectrum within the wavelength range of $\lambda > 4,900$ Å, which was free from the stray light (see Paper I for its detail). We ignore the effect of the atmospheric refraction here because we only use a red side ($\lambda > 4,900$ Å) of DEIMOS data, which is insensitive to the atmospheric refraction. We also confirm that the effect of the atmospheric refraction is negligible with the models described in Section 3.1. In the DEIMOS data, we only used line flux ratios normalized to an $H\beta$ flux. Emission line fluxes were scaled with an $H\beta$ flux by matching an $H\beta$ flux obtained with DEIMOS to one obtained with FOCAS (see Section 3.4).

3.4. Subaru/FOCAS

We carried out deep spectroscopy for one galaxy selected from our HSC catalog (HSC J1631+4426) with FOCAS installed on the Subaru telescope (PI: T. Kojima). This object was the same object as in the Keck/DEIMOS Spectroscopy (Section 3.3) and observed again with FOCAS with a longer integration time of 10,800 sec. We used the long slit mode with the $2''$ slit width. The exposure time was 10,800 seconds ($=3$

hours). We used the 300R grism and the L550 filter with a blaze wavelength at 7,500 Å in a 2nd order. The FOCAS spectroscopy covered $\lambda \sim 3,400\text{--}5,250$ Å with a spectral resolution of $R \equiv \lambda/\Delta\lambda = 400$ with the $2''$ slit width.

We used the IRAF package to reduce and calibrate the FOCAS data. The reduction and calibration processes were the same as the LDSS-3 data explained in Section 3.1. A standard star, BD+28 4211 was used in the flux calibration. Wavelengths were calibrated with the ThAr lamp. Atmospheric absorption was corrected in the same way as in Section 3.3. Our FOCAS spectroscopy covered $\lambda \sim 3,800\text{--}5,250$ Å, which was complementary to the DEIMOS spectroscopy described in Section 3.3, whose spectrum was reliable only in the range of $\lambda > 4900$ Å. We ignore the atmospheric refraction here because FOCAS is equipped with the atmospheric dispersion corrector. Because an $H\beta$ line was over-wrapped in FOCAS and DEIMOS spectroscopy, we used an $H\beta$ line flux to scale the emission line fluxes obtained in the DEIMOS observation (see Section 3.3).

3.5. Weak Emission Lines in the Spectra

In our spectroscopy, we have detected many emission lines including very faint emission lines such as [O III]4363, [Ar IV]4711, [Fe III]4658, He II4686, [N II]6584, and [Ar III]7136. These faint emission lines are required to estimate element abundance ratios and constrain the FUV spectral hardness. Especially, the [Fe III]4658 and He II4686 lines are key in this paper, which enable us to investigate the Fe/O abundance ratios and the very hard EUV radiation, as described in Section 1.

In Figure 1, we show two spectra of SDSS J2115–1734 and HSC J1631+4426 (classified as EMPGs in Paper I) around the [Fe III]4658 and He II4686 emission lines. In the left panel of Figure 1, the spectrum of SDSS J2115–1734 clearly exhibits the significant detection of the [Fe III]4658 and He II4686 emission lines. As shown in the right panel, the HSC J1631+4426 spectrum shows the significant detection of He II4686 ($S/N=6.1$) as well as the tentative detection of [Fe III]4658 ($S/N=2.4$). The flux measurements will be described in Section 4.1.

As described above, we also include the EMPG, J0811+4730 of $0.019 Z_{\odot}$ in the sample of this paper. In Figure 2, we show a spectrum of J0811+4730 derived from Izotov et al. (2018), showing the detection of the two key emission lines of [Fe III]4658 and He II4686 in this paper.

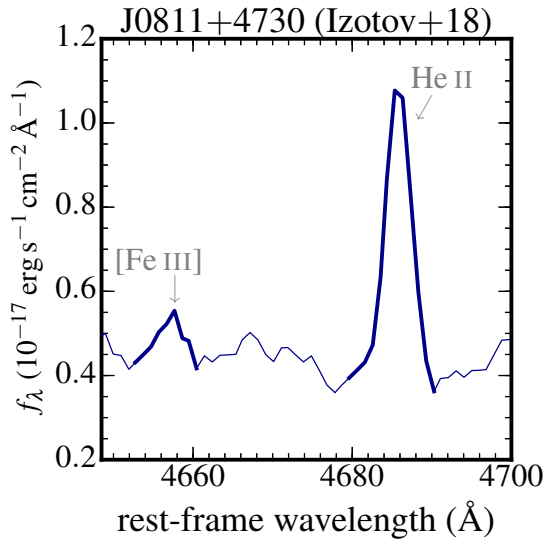


FIG. 2.— Spectrum of J0811+4730 (Izotov et al. 2018) around the [Fe III]4658 and He II4686 emission lines. This spectrum was taken with Multi-Object Double Spectrographs (MODS) installed on Large Binocular Telescope (LBT). This spectrum is adapted from Izotov et al. (2018) with permission.

4. ANALYSIS

In this section, we explain the emission line measurement (Section 4.1) and the estimation of galaxy properties (Section 4.2) for our 10 metal-poor galaxies. Here we estimate stellar masses, star-formation rates, emission-line equivalent widths, sizes, and metallicities of our 10 metal-poor galaxies.

4.1. Emission Line Measurements

We measure central wavelengths and emission-line fluxes with a best-fit gaussian profile using the IRAF routine, `splot`. We also estimate flux errors, which originate from read-out noise and photon noise of sky+object emission. As described in Section 3.2, we correct fluxes of the LDSS-3/MagE spectra assuming the wavelength-dependent slit-loss with the model of the atmospheric refraction. We measure observed-frame equivalent widths (EWs) of emission lines with the same IRAF routine, `splot` and convert them into the rest-frame equivalent widths (EW_0). Redshifts are estimated by comparing the

observed central wavelengths and the rest-frame wavelengths in the air of strong emission lines.

Color excesses, $E(B-V)$ are estimated with the Balmer decrement of H α , H β , H γ , H δ ,..., and H13 lines under the assumptions of the dust extinction curve given by Cardelli et al. (1989) and the case B recombination. We do not use Balmer emission lines affected by a systematic error such as cosmic rays and other emission lines blending with the Balmer line. In the case B recombination, we carefully assume electron temperatures (T_e) so that the assumed electron temperatures become consistent with electron temperature measurements of O $^{2+}$, $T_e(\text{O III})$, which will be obtained in Section 4.2. We estimate the best $E(B-V)$ values and their errors with the χ^2 method (Press et al. 2007). The $E(B-V)$ estimation process is detailed in Paper I. We eventually assume $T_e=10,000$ K (SDSS J0002+1715 and SDSS J1642+2233), 15,000 K (HSC J1429–0110, HSC J2314+0154, SDSS J2253+1116, SDSS J2310–0211, and SDSS J2327–0200), 20,000 K (HSC J1142–0038 and SDSS J2115–1734), 25,000 K (HSC J1631+4426), which are roughly consistent with $T_e(\text{O III})$ measurements. We summarize the dust-corrected fluxes in Table 1.

4.2. Galaxy Properties

In this section, we estimate gas-phase metallicities (O/H), and gas-phase element abundance ratios of our 10 galaxies. Note that metallicities are already estimated in Paper I, as well as stellar masses, SFRs, and color excesses.

We estimate electron temperatures of O $^{2+}$ ($T_e(\text{O III})$) and O $^{+}$ ($T_e(\text{O II})$), using line ratios of [O III]4363/5007 and [O II](3727+3729)/(7320+7330), respectively. We use nebular physics calculation codes of PyNeb (Luridiana et al. 2015, v1.0.14) to estimate electron temperatures. If an [O II]5007 line is saturated, we estimate an [O II]5007 flux with

$$[\text{O III}]5007 = 2.98 \times [\text{O III}]4959, \quad (1)$$

which is strictly determined by the Einstein A coefficient. If either of [O II]7320 or [O II]7330 line is detected, we estimate a total flux of [O II](7320+7330) with a relation of

$$[\text{O II}]7330 = 0.56 \times [\text{O II}]7320. \quad (2)$$

We have confirmed that Equation (2) holds with very little dependence on T_e and n_e , using PyNeb. If none of [O II]7320,7330 line is detected, we estimate $T_e(\text{O II})$ from an empirical relation of

$$T_e(\text{O II}) = 0.7 \times T_e(\text{O III}) + 3000, \quad (3)$$

which has been confirmed by Campbell et al. (1986) and Garnett (1992). We also assume

$$T_e(\text{S III}) = 0.83 \times T_e(\text{O III}) + 1700, \quad (4)$$

to estimate electron temperatures associated with S $^{2+}$ ions (Garnett 1992). We regard $T_e(\text{O III})$, $T_e(\text{S III})$, and $T_e(\text{O II})$ as representative electron temperatures associated with ions in high, intermediate, and low ionization states, respectively.

We estimate gas-phase metallicities, $12+\log(\text{O}/\text{H})$, based on electron temperature measurements, which are

TABLE 1
FLUX MEASUREMENTS

# (1)	ID (2)	[O II]3727 (3)	[O II]3729 (4)	[O II] _{tot} (5)	H13 (6)	H12 (7)	H11 (8)	H10 (9)	H9 (10)
1	HSC J1429−0110	—	—	160.33±1.91	<1.27	<0.93	<0.89	<0.79	5.26±0.66
2	HSC J2314+0154	<14.09	<13.38	<19.43	<11.93	<10.42	<11.48	<8.06	<6.77
3	HSC J1142−0038	68.06±0.81	91.82±0.84	159.88±1.16	3.26±0.68	3.63±0.67	6.65±0.79	4.39±0.66	6.13±0.63
4	HSC J1631+4426	—	—	41.91±2.22	<1.49	<1.34	<1.18	<1.14	3.96±0.99
5	SDSS J0002+1715	74.28±0.50	103.08±0.51	177.36±0.71	<0.33	<0.49	<0.36	5.99±0.30	8.42±0.25
6	SDSS J1642+2233	101.37±0.71	146.56±0.74	247.93±1.03	<0.48	<0.46	<0.74	<0.41	6.62±0.33
7	SDSS J2115−1734	31.36±0.25	43.15±0.28	74.51±0.38	2.58±0.19	3.16±0.30	3.91±0.19	4.07±0.18	5.44±0.17
8	SDSS J2253+1116	39.44±0.11	55.06±0.12	94.50±0.16	2.36±0.06	3.40±0.05	4.08±0.05	5.59±0.05	7.59±0.05
9	SDSS J2310−0211	43.37±0.10	58.68±0.12	102.05±0.16	2.36±0.06	2.73±0.06	3.75±0.06	5.68±0.06	7.44±0.06
10	SDSS J2327−0200	45.07±0.11	59.96±0.12	105.03±0.16	2.48±0.06	3.36±0.06	3.99±0.08	5.29±0.06	7.19±0.06
# (1)	[Ne III]3869 (11)	[Ne III]3967 (12)	H7 (13)	Hδ (14)	Hγ (15)	[O III]4363 (16)	[Fe III]4658 (17)	HeII4686 (18)	[Ar IV]4711 (19)
1	61.78±0.68	—	31.46±0.46 ^a	21.05±0.32	44.71±0.27	8.90±0.22	0.93±0.17	1.36±0.17	2.00±0.16
2	<5.83	<3.87	<3.83	25.99±3.09	46.36±1.66	<1.60	<1.14	<1.04	<0.94
3	29.33±0.63	7.74±0.54	17.16±0.54	27.36±0.51	48.20±0.43	5.96±0.39	<0.29	<0.30	<0.41
4	18.48±0.95	—	17.28±0.75 ^a	24.24±0.57	42.98±0.45	7.53±0.44	0.89±0.37	2.26±0.37	<0.34
5	46.64±0.30	15.00±0.21	16.27±0.19	26.04±0.17	46.92±0.14	6.38±0.09	0.66±0.05	0.86±0.05	0.79±0.06
6	43.87±0.36	12.00±0.25	15.03±0.24	26.08±0.19	44.48±0.16	6.54±0.10	0.64±0.06	1.20±0.06	0.44±0.11
7	40.46±0.22	13.05±0.16	14.52±0.15	24.63±0.15	45.15±0.15	13.42±0.11	0.86±0.06	2.63±0.11	1.87±0.08
8	64.12±0.11	18.82±0.06	16.12±0.06	25.67±0.05	46.52±0.06	14.13±0.04	0.36±0.01	0.30±0.02	2.12±0.02
9	53.18±0.10	15.76±0.06	16.28±0.06	26.52±0.06	48.39±0.07	14.80±0.04	0.45±0.02	0.48±0.02	1.70±0.02
10	50.72±0.11	15.14±0.07	17.45±0.07	25.93±0.07	47.39±0.08	12.81±0.05	0.63±0.03	0.78±0.03	1.51±0.03

NOTE. — (1): Number. (2): ID. (3)–(36): Dust-corrected emission-line fluxes normalized to an H β line flux in the unit of erg s^{−1} cm^{−2}. Upper limits are given with a 1 σ level. Lines suffering from saturation or affected by sky emission lines are shown as no data here. [O II]_{tot} represents a sum of [O II]3727 and [O II]3729 fluxes. If the spectral resolution is not high enough to resolve [O II]3727 and [O II]3729 lines, we only show [O II]_{tot} fluxes.

^a A sum of [Ne III]3867 and H7 fluxes because they are blended due to the low spectral resolution.

TABLE 1
FLUX MEASUREMENTS — *Continued*

# (1)	ID (2)	[Ar IV]4740 (20)	H β (21)	[O III]4959 (22)	[O III]5007 (23)	HeI5876 (24)	[O I]6300 (25)	[S III]6312 (26)	[N II]6548 (27)
1	HSC J1429–0110	0.95 \pm 0.16	100.00 \pm 0.24	211.26 \pm 0.29	629.72 \pm 0.46	9.51 \pm 0.09	3.04 \pm 0.08	1.10 \pm 0.08	<0.20
2	HSC J2314+0154	<1.01	100.00 \pm 1.00	69.62 \pm 0.72	207.69 \pm 0.88	12.92 \pm 0.41	11.96 \pm 0.49	<0.44	<0.32
3	HSC J1142–0038	<0.36	100.00 \pm 0.52	102.76 \pm 0.47	308.14 \pm 0.65	11.11 \pm 0.31	5.29 \pm 0.31	<0.30	1.99 \pm 0.24
4	HSC J1631+4426	<0.35	100.00 \pm 0.37	56.56 \pm 0.34	174.53 \pm 0.39	10.21 \pm 0.67	—	<0.63	<0.59
5	SDSS J0002+1715	0.88 \pm 0.06	100.00 \pm 0.16	196.65 \pm 0.19	593.18 \pm 0.32	11.09 \pm 0.05	2.34 \pm 0.04	1.63 \pm 0.03	1.92 \pm 0.03
6	SDSS J1642+2233	0.78 \pm 0.07	100.00 \pm 0.17	183.53 \pm 0.21	572.88 \pm 0.34	10.87 \pm 0.06	2.63 \pm 0.04	1.91 \pm 0.04	1.71 \pm 0.04
7	SDSS J2115–1734	1.73 \pm 0.07	100.00 \pm 0.19	166.56 \pm 0.22	—	11.38 \pm 0.07	1.82 \pm 0.05	1.83 \pm 0.05	1.28 \pm 0.04
8	SDSS J2253+1116	1.69 \pm 0.02	100.00 \pm 0.07	250.60 \pm 0.11	—	11.17 \pm 0.02	—	—	1.16 \pm 0.01
9	SDSS J2310–0211	1.39 \pm 0.02	100.00 \pm 0.09	214.45 \pm 0.12	—	10.46 \pm 0.03	2.41 \pm 0.02	1.24 \pm 0.02	1.07 \pm 0.02
10	SDSS J2327–0200	1.12 \pm 0.03	100.00 \pm 0.11	200.95 \pm 0.14	—	11.28 \pm 0.04	2.79 \pm 0.03	1.52 \pm 0.02	1.31 \pm 0.02
# (1)	H α (28)	[N II]6584 (29)	HeI6678 (30)	[S II]6716 (31)	[S II]6731 (32)	HeI7065 (33)	[Ar III]7136 (34)	[O II]7320 (35)	[O II]7330 (36)
1	255.60 \pm 0.20	5.27 \pm 0.18	3.07 \pm 0.07	8.17 \pm 0.08	6.31 \pm 0.09	2.85 \pm 0.08	5.88 \pm 0.08	1.53 \pm 0.07	0.97 \pm 0.07
2	280.66 \pm 0.67	2.12 \pm 0.30	—	5.22 \pm 0.33	<0.55	—	<0.86	<0.47	<0.62
3	272.09 \pm 0.57	8.64 \pm 0.26	2.75 \pm 0.21	16.24 \pm 0.24	8.52 \pm 0.27	<0.30	5.52 \pm 0.43	<0.36	<0.37
4	270.67 \pm 1.17	<0.57	2.47 \pm 0.70	—	—	—	—	<0.60	<0.68
5	280.48 \pm 0.17	5.68 \pm 0.04	2.99 \pm 0.03	11.19 \pm 0.04	5.97 \pm 0.03	2.58 \pm 0.03	—	—	—
6	281.31 \pm 0.21	5.38 \pm 0.04	2.69 \pm 0.04	10.59 \pm 0.06	8.30 \pm 0.04	1.45 \pm 0.04	6.44 \pm 0.05	1.89 \pm 0.04	1.50 \pm 0.04
7	300.97 \pm 0.24	3.36 \pm 0.04	—	5.67 \pm 0.04	5.06 \pm 0.05	3.97 \pm 0.05	5.08 \pm 0.07	1.20 \pm 0.05	0.92 \pm 0.04
8	—	3.29 \pm 0.01	2.97 \pm 0.01	6.47 \pm 0.01	5.07 \pm 0.01	3.56 \pm 0.01	5.08 \pm 0.02	1.55 \pm 0.01	1.03 \pm 0.01
9	—	2.78 \pm 0.02	2.67 \pm 0.02	7.70 \pm 0.02	5.60 \pm 0.02	3.21 \pm 0.02	4.74 \pm 0.02	1.28 \pm 0.02	0.99 \pm 0.02
10	—	3.21 \pm 0.02	2.93 \pm 0.02	8.78 \pm 0.03	6.49 \pm 0.03	3.83 \pm 0.03	5.36 \pm 0.03	1.69 \pm 0.02	—

NOTE. — Continued.

TABLE 2
PARAMETERS OF OUR METAL-POOR GALAXIES

#	ID	EMPG?	redshift	EW ₀ (H β)	12+log(O/H)	log(M_{\star})	log(SFR)	$E(B-V)$
(1)	(2)	(3)	(4)	(\AA) (5)	(6)	(M_{\odot}) (7)	($M_{\odot} \text{ yr}^{-1}$) (8)	(mag) (9)
1	HSC J1429–0110	<i>no</i>	0.02980	172.6 $^{+0.7}_{-0.6}$	8.27 \pm 0.02	6.55 $^{+0.13}_{-0.09}$	0.43 \pm 0.01	0.35 \pm 0.02
2	HSC J2314+0154	<i>yes</i> ^a	0.03265	213.3 $^{+23.4}_{-17.6}$	7.23 $^{+0.03}_{-0.02}$ ^a	5.17 \pm 0.01	–0.85 \pm 0.01	0.28 \pm 0.03
3	HSC J1142–0038	<i>no</i>	0.02035	111.9 $^{+1.4}_{-1.3}$	7.72 \pm 0.03	4.95 $^{+0.04}_{-0.01}$	–1.07 \pm 0.01	0.00 $^{+0.02}_{-0.00}$
4	HSC J1631+4426	<i>yes</i>	0.03125	123.5 $^{+3.5}_{-2.8}$	6.90 \pm 0.03	5.89 $^{+0.10}_{-0.09}$	–1.28 \pm 0.01	0.19 \pm 0.03
5	SDSS J0002+1715	<i>no</i>	0.02083	103.9 \pm 0.2	8.22 \pm 0.01	7.06 \pm 0.03	0.00 \pm 0.01	0.00 $^{+0.01}_{-0.00}$
6	SDSS J1642+2233	<i>no</i>	0.01725	153.7 $^{+0.5}_{-0.4}$	8.45 \pm 0.01	6.06 $^{+0.03}_{-0.13}$	–0.17 \pm 0.01	0.02 \pm 0.02
7	SDSS J2115–1734	<i>yes</i>	0.02296	214.0 $^{+0.9}_{-0.8}$	7.68 \pm 0.01	6.56 \pm 0.02	0.27 \pm 0.01	0.19 \pm 0.03
8	SDSS J2253+1116	<i>no</i>	0.00730	264.7 \pm 0.3	7.973 \pm 0.002	5.78 \pm 0.01	–0.54 \pm 0.01	0.00 $^{+0.01}_{-0.00}$
9	SDSS J2310–0211	<i>no</i>	0.01245	127.6 \pm 0.2	7.890 $^{+0.003}_{-0.004}$	6.99 \pm 0.03	–0.16 \pm 0.01	0.01 $^{+0.02}_{-0.01}$
10	SDSS J2327–0200	<i>no</i>	0.01812	111.0 \pm 0.2	7.866 $^{+0.004}_{-0.005}$	6.51 $^{+0.02}_{-0.03}$	–0.18 \pm 0.01	0.00 $^{+0.02}_{-0.00}$

NOTE. — (1): Number. (2): ID. (3): Whether or not an object satisfies the EMPG definition, 12+log(O/H) < 7.69. If yes (no), we write *yes* (*no*) in the column. (5): Rest-frame equivalent width of an H β emission line. (6): Gas-phase metallicity based on the T_e method except for HSC J2314+0154. (7): Stellar mass. (8): Star-formation rate. (9): Color excess.

^a The metallicity of HSC J2314+0154 is obtained with the metallicity calibration of Skillman (1989).

so-called T_e -metallicities. Hereafter, we call the T_e -metallicity just “metallicity” unless we describe explicitly. We also use PyNeb to estimate metallicities. The latest atomic data are used in the PyNeb codes. We do not estimate a T_e -based metallicity of HSC J2314+0154 because none of the $T_e(\text{OIII})$, $T_e(\text{OII})$, and $T_e(\text{SIII})$ is estimated due to non-detection of [O III]4363 and [O II]7320,7330 emission lines. Instead, we estimate the metallicity of HSC J2314+0154 with a calibrator obtained by Skillman (1989) as described in Paper I. The estimates of gas-phase metallicities are summarized in Table 2. The estimation of electron temperatures and metallicities are detailed in Paper I.

We estimate gas-phase element abundance ratios of neon-to-oxygen (Ne/O), argon-to-oxygen (Ar/O), nitrogen-to-oxygen (N/O), and iron-to-oxygen (Fe/O) in a similar way to Izotov et al. (2006). First, we estimate ion abundance ratios of Ne $^{2+}$ /H $^{+}$, Ar $^{3+}$ /H $^{+}$, Ar $^{2+}$ /H $^{+}$, N $^{+}$ /H $^{+}$, and, Fe $^{2+}$ /H $^{+}$ with the PyNeb codes. Because different ions reside in different parts of an H II region, we choose one of the $T_e(\text{OIII})$, $T_e(\text{SIII})$, and $T_e(\text{OII})$ to estimate abundances of each ion according to their ionization potential. We use $T_e(\text{OIII})$ to estimate abundances of O $^{2+}$, Ne $^{2+}$, and Ar $^{3+}$. We adopt $T_e(\text{SIII})$ in the estimation of Ar $^{2+}$ abundances. We apply $T_e(\text{OII})$ for abundances of low-ionization ions, O $^{+}$, N $^{+}$, and Fe $^{2+}$. Second, we convert the ion abundances into element abundances with ionization correction factors ($ICFs$) of Izotov et al. (2006) shown below:

$$\frac{\text{Ne}}{\text{H}} = \frac{\text{Ne}^{+}}{\text{H}^{+}} + ICF(\text{Ne}^{+}), \quad (5)$$

$$\frac{\text{Ar}}{\text{H}} = \frac{\text{Ar}^{3+} + \text{Ar}^{2+}}{\text{H}^{+}} + ICF(\text{Ar}^{3+} + \text{Ar}^{2+}), \quad (6)$$

$$\frac{\text{N}}{\text{H}} = \frac{\text{N}^{+}}{\text{H}^{+}} + ICF(\text{N}^{+}), \quad (7)$$

$$\frac{\text{Fe}}{\text{H}} = \frac{\text{Fe}^{2+}}{\text{H}^{+}} + ICF(\text{Fe}^{2+}). \quad (8)$$

The $ICFs$ are based on H II region models of Stasińska & Izotov (2003) and are given as a function

of $v = \text{O}^{+}/(\text{O}^{2+} + \text{O}^{+})$ or $w = \text{O}^{2+}/(\text{O}^{2+} + \text{O}^{+})$. Finally, we obtain Ne/O, Ar/O, N/O, and Fe/O ratios by dividing Ne/H, Ar/H, N/H, and Fe/H by O/H (i.e., metallicity). We do not estimate Ne/O, Ar/O, N/O, and Fe/O ratios of HSC J2314+0154 because none of the $T_e(\text{OIII})$, $T_e(\text{OII})$, and $T_e(\text{SIII})$ is obtained. The Ar/O ratios of HSC J1631+4426 and SDSS J0002+1715 are not estimated as well because the [Ar III]7136 emission line is strongly affected by the sky emission line. For the literature EMPG, J0811+4730, we derive the element abundances from Izotov et al. (2018). The element abundances of J0811+4730 are obtained in the same manner as in this paper. We summarize the element abundance ratios in Table 3.

5. RESULTS AND DISCUSSIONS

5.1. Element Abundance Ratios

We show the element abundance ratios of neon, argon, nitrogen, and iron to oxygen (Ne/O, Ar/O, N/O, and Fe/O) of our metal-poor galaxy sample consisting of 10 metal-poor galaxies from Paper I and J0811+4730 from Izotov et al. (2018). Figure 3 shows the Ne/O, Ar/O, N/O, and Fe/O ratios as a function of metallicity, 12+log(O/H). Thanks to the two representative EMPGs, HSC J1631+4426 (0.016 Z_{\odot}) and J0811+4730 (0.019 Z_{\odot}), we are able to investigate and discuss the low metallicity end (below 0.02 Z_{\odot}) of the element abundances for the first time. We discuss these element abundance ratios in the following subsections. We compare the element abundance ratios of our metal-poor galaxy sample with a metal-poor galaxy sample of Izotov et al. (2006), whose typical stellar mass range is larger than our sample galaxies.

5.1.1. Ne/O and Ar/O ratios

Izotov et al. (2006) report that Ne/O and Ar/O ratios little depend on metallicity because the neon, argon, and oxygen are all α elements, which are produced by the nuclear fusion of α particles inside stars. As shown in the panels (a) and (b) of Figure 3, we find that our metal-poor galaxy sample shows almost constant values

TABLE 3
ELEMENT ABUNDANCE RATIOS

# (1)	ID (2)	$\log(\text{Ne}/\text{O})$ (3)	$\log(\text{Ar}/\text{O})$ (4)	$\log(\text{N}/\text{O})$ (5)	$\log(\text{Fe}/\text{O})$ (6)
1	HSC J1429–0110	$-0.634^{+0.006}_{-0.007}$	$-2.634^{+0.028}_{-0.026}$	$-1.753^{+0.020}_{-0.023}$	$-1.994^{+0.091}_{-0.075}$
2	HSC J2314+0154	— ^a	— ^a	— ^a	— ^a
3	HSC J1142–0038	$-0.712^{+0.008}_{-0.010}$	< -2.253	$-1.297^{+0.019}_{-0.014}$	< -2.124
4	HSC J1631+4426	$-0.641^{+0.022}_{-0.019}$	— ^b	< -1.710	$-1.246^{+0.174}_{-0.313}$
5	SDSS J0002+1715	$-0.701^{+0.003}_{-0.002}$	— ^b	-1.644 ± 0.004	$-2.126^{+0.035}_{-0.027}$
6	SDSS J1642+2233	-0.754 ± 0.005	$-2.704^{+0.016}_{-0.015}$	$-1.943^{+0.006}_{-0.009}$	$-2.335^{+0.027}_{-0.038}$
7	SDSS J2115–1734	$-0.757^{+0.005}_{-0.004}$	$-2.274^{+0.007}_{-0.013}$	$-1.518^{+0.009}_{-0.011}$	-1.639 ± 0.026
8	SDSS J2253+1116	-0.707 ± 0.001	-2.391 ± 0.002	-1.563 ± 0.003	$-2.078^{+0.020}_{-0.022}$
9	SDSS J2310–0211	-0.761 ± 0.001	-2.440 ± 0.004	$-1.710^{+0.005}_{-0.004}$	$-2.046^{+0.019}_{-0.023}$
10	SDSS J2327–0200	$-0.737^{+0.001}_{-0.002}$	-2.386 ± 0.006	$-1.616^{+0.006}_{-0.004}$	$-1.890^{+0.022}_{-0.017}$

NOTE. — (1): Number. (2): ID. (3)–(6): Gas-phase element abundance ratios of Ne/O, Ar/O, N/O, and Fe/O. Upper limits are given with a 2σ confidence level.

^a Not estimated due to the lack of electron temperature estimates.

^b Not estimated because the [Ar III]7136 emission line is strongly affected by the sky emission line.

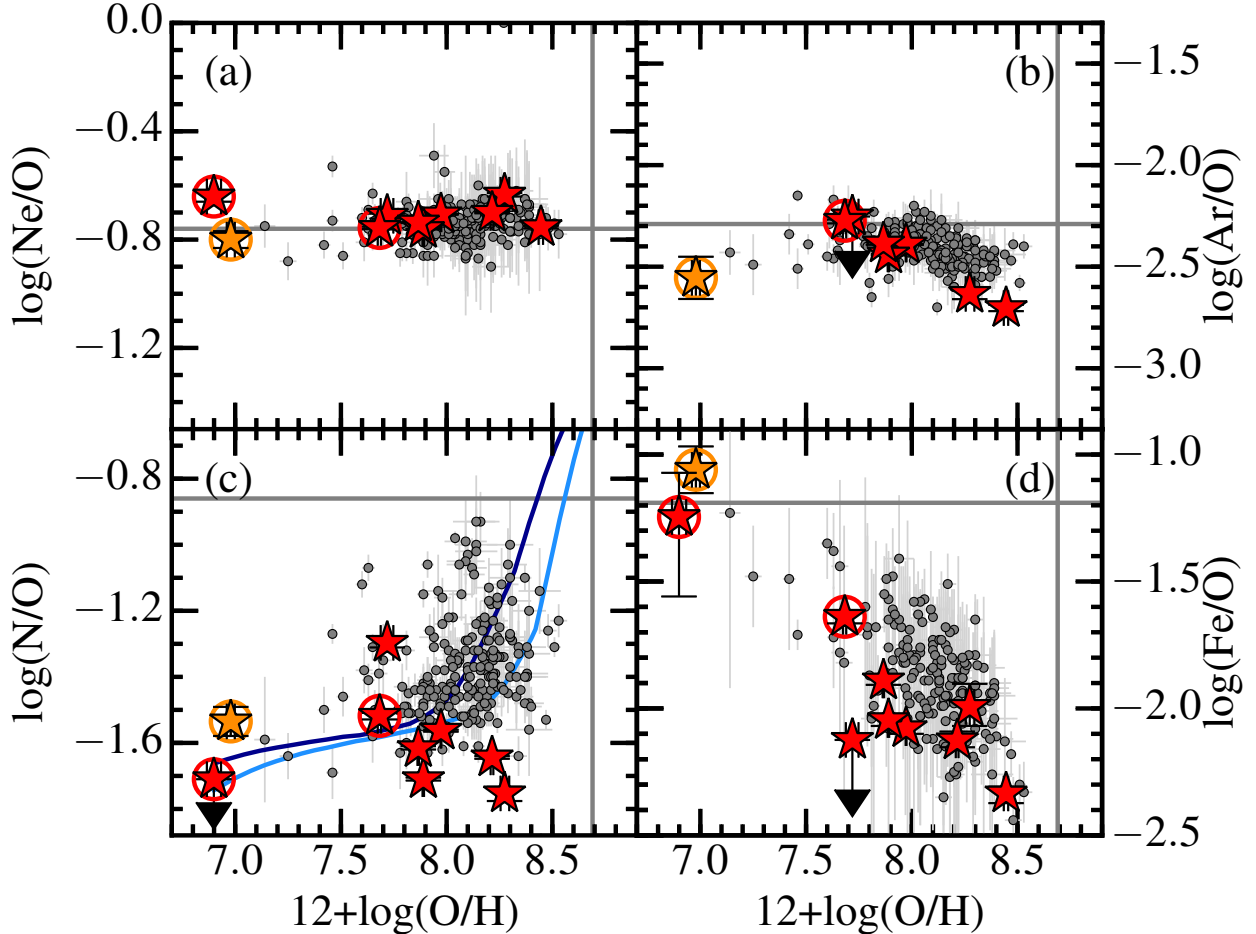


FIG. 3.— Element abundance ratios of neon, argon, nitrogen, and iron to oxygen (Ne/O, Ar/O, N/O, and Fe/O) are shown as a function of metallicity in the panels (a) to (d), respectively. Our metal-poor galaxies from HSC-EMPG and SDSS-EMPG source catalogs are shown with red stars. The EMPG, J0811+4730, which is derived from Izotov et al. (2018) is shown with the orange star. Metal-poor galaxies that satisfy the EMPG are marked with a large circle. Here we do not show HSC J2314+0154, whose T_e -metallicity and element abundances are not estimated due to the lack of the electron temperature measurement. Gray dots represent local galaxies of Izotov et al. (2006). Gray vertical and horizontal lines indicate solar abundance ratios and metallicity (Asplund et al. 2009). Solid lines in the panel (c) are the model calculations of the N/O evolution (Vincenzo et al. 2016) with star-formation efficiencies of 0.5 (dark blue) and 1.0 (light blue) Gyr^{-1} . The Ar/O ratios of HSC J1631+4426 and SDSS J0002+1715 are not shown here because the [Ar III]7136 emission line is strongly affected by the sky emission line.

of $\log(\text{Ne}/\text{O}) \sim -0.8$ and $\log(\text{Ar}/\text{O}) \sim -2.5$ within a scatter of ± 0.2 dex, which are almost consistent with the solar abundance ratios. We also find that the Ne/O and Ar/O ratios are consistent with those of local galaxies reported by Izotov et al. (2006) within the scatter. The consistency suggests that our metal-poor galaxy sample also shows no metallicity dependence in Ne/O and Ar/O ratios.

Note that the Ar/O ratio might slightly decrease in the range of $12 + \log(\text{O}/\text{H}) \gtrsim 8.2$ in our sample and the Izotov et al. (2006) sample, in contrast to the Ne/O ratios. The Ar/O ratio is expected to be constant and consistent with the solar abundance, $\log(\text{Ar}/\text{O})_{\odot} = -2.29$, because there seems to be no physical reason for the Ar/O (i.e., α element ratio) decrease at $12 + \log(\text{O}/\text{H}) \gtrsim 8.2$. It may be explained by the underlying unknown systematics in the Ar/O estimation at $12 + \log(\text{O}/\text{H}) \gtrsim 8.2$. We do not discuss it further in this paper because the Ar/O abundances at relatively higher metallicities are out of the scope of this paper.

5.1.2. N/O ratio

As suggested by previous studies (Pérez-Montero & Contini 2009; Pérez-Montero et al. 2013; Andrews & Martini 2013), N/O ratios of SFGs present a plateau at $\log(\text{N}/\text{O}) \sim -1.6$ in the range of $12 + \log(\text{O}/\text{H}) \lesssim 8.0$ and a positive slope at higher metallicities as a function of metallicity. The panel (c) of Figure 3 presents model calculations of the N/O evolution (Vincenzo et al. 2016), which also show the plateau and positive slope. The plateau basically results from the primary nucleosynthesis of massive stars, while the positive slope is mainly attributed to the secondary nucleosynthesis of low- and intermediate-mass stars (e.g., Vincenzo et al. 2016). We briefly describe the two nitrogen production processes below.

- Primary nucleosynthesis: Inside a metal-poor star, protons are burned through the proton-proton (p - p) chain reaction, and little nitrogen is produced at this stage. Nitrogen elements are mainly produced after the formation of a heavy-element core (e.g., O and C) and ejected into ISM by SNe, for stars more massive than $\sim 8 M_{\odot}$.
- Secondary nucleosynthesis: Metal-rich stars efficiently burn hydrogen through the carbon-nitrogen-oxygen (CNO) cycle, where nitrogen elements accumulate because ^{14}N fusion ($^{14}\text{N} + p \rightarrow ^{15}\text{O} + \gamma$) is the slowest process in the CNO cycle. Then nitrogen is ejected through stellar winds during the asymptotic giant branch (AGB) phase, ~ 1 Gyr after the birth of low- and intermediate-mass stars.

As shown in the panel (c) of Figure 3, most of our metal-poor galaxies have N/O ratios of $\log(\text{N}/\text{O}) < -1.5$ (i.e., less than ~ 30 percent of the solar N/O ratio). Especially, HSC J1631+4426 has a strong, 2σ upper limit of $\log(\text{N}/\text{O}) < -1.71$, and J0811+4730 show a low N/O ratio of $\log(\text{N}/\text{O}) = -1.53$. The N/O values of the two EMPGs (HSC J1631+4426 and J0811+4730) will be discussed again in Section 5.1.3. These low N/O ratios suggest that our metal-poor galaxies have not yet started the

secondary nucleosynthesis due to their low metallicities and young stellar ages.

We also find several galaxies of our metal-poor galaxy sample have relatively low N/O ratios compared to the model lines of Vincenzo et al. (2016) and Izotov et al. (2006) SFGs at $12 + \log(\text{O}/\text{H}) \sim 8.0$. Vincenzo et al. (2016) find that the N/O plateau is lowered under the assumption of high sSFR or the top heavy initial mass function (IMF). Indeed, our metal-poor galaxy sample have high sSFRs ($\sim 300 \text{ Gyr}^{-1}$) compared to those of the Izotov et al. (2006) SFGs ($\sim 1\text{--}10 \text{ Gyr}^{-1}$) because we aim to obtain galaxies with high sSFRs in this study. Thus, the N/O differences between our metal-poor galaxy sample and Izotov et al. (2006) SFG sample are explained by the sample selection.

5.1.3. Fe/O ratio

In the panel (d) of Figure 3, we find that our metal-poor galaxies show a decreasing trend in Fe/O ratio as metallicity increases. The same decreasing Fe/O trend is found in a star-forming-galaxy sample of Izotov et al. (2006). Most of our metal-poor galaxies have Fe/O ratios comparable to a star-forming-galaxy sample of Izotov et al. (2006). Three EMPGs, HSC J1631+4426, SDSS J2115-1734, and J0811+4730 (encircled by a red or orange circle) show relatively high Fe/O ratios, $\log(\text{Fe}/\text{O}) > -1.7$, among our metal-poor galaxies. Especially, we find that HSC J1631+4426 and J0811+4730, two of the lowest metallicity galaxies with 0.016 and 0.019 $(\text{O}/\text{H})_{\odot}$, have high Fe/O ratios of $\log(\text{Fe}/\text{O}) = -1.25^{+0.17}_{-0.31}$ and $\log(\text{Fe}/\text{O}) = -1.06 \pm 0.09$, respectively, which are comparable to the solar Fe/O ratio, $\log(\text{Fe}/\text{O})_{\odot} = -1.19$. In this paper, we mainly focus on the two representative EMPGs, HSC J1631+4426 and J0811+4730, which interestingly show high Fe/O ratios. Note again that J0811+4730 is an EMPG reported by Izotov et al. (2018). Table 4 summarizes the Fe/O ratios and He II $\lambda 4686/\text{H}\beta$ ratios (discussed in Section 5.2.2) of the two representative EMPGs (HSC J1631+4426 and J0811+4730), which play an important role in this paper. We also show the fluxes of the two key emission lines of [Fe III] $\lambda 4658$ and He II $\lambda 4686$ in Table 4.

To characterize the two EMPGs (HSC J1631+4426 and J0811+4730) with a high Fe/O ratio, we also compare our metal-poor galaxies with Galactic stars (Cayrel et al. 2004; Gratton et al. 2003; Bensby et al. 2013) in Figure 4. The Galactic star samples are composed of dwarf or subdwarf stars. The solid line here represents a stellar Fe/O evolution model under the assumption that gas is enriched by massive stars with $9\text{--}100 M_{\odot}$ (Suzuki & Maeda 2018). The gaseous abundance ratios at the time of the star formation are imprinted in the stellar abundance patterns because stars are formed from gas. As explained in Section 1, the Fe/O ratio increases at $12 + \log(\text{O}/\text{H}) \gtrsim 8.0$ due to the contribution of type-Ia SNe ~ 1 Gyr after the start of the star formation. Surprisingly, we find in Figure 4 that the two EMPGs (HSC J1631+4426 and J0811+4730) deviate from the observational results of Galactic stars and the Fe/O evolution model. Below, we mainly focus on the discussion of the two EMPGs of HSC J1631+4426 and J0811+4730, unless we specifically describe explicitly. Note that our metal-poor galaxies present gas-phase Fe/O ratios in nebulae,

TABLE 4
PARAMETERS OF TWO REPRESENTATIVE EMPGs

ID	$12+\log(\text{O}/\text{H})$	$\log(\text{Fe}/\text{O})$	$\log(\text{He II}/\text{H}\beta)$	$F([\text{Fe III}])$ ($\text{erg s}^{-1} \text{cm}^{-2}$)	$F(\text{He II})$ ($\text{erg s}^{-1} \text{cm}^{-2}$)	Ref.
(1)	(2)	(3)	(4)	(5)	(6)	(7)
HSC J1631+4426	6.90 ± 0.03	$-1.25^{+0.17}_{-0.31}$	$-1.58^{+0.07}_{-0.08}$	12.0 ± 5.02	30.5 ± 5.04	This paper
J0811+4730	6.98 ± 0.02	-1.06 ± 0.09	-1.64 ± 0.03	6.55 ± 1.26	28.6 ± 1.89	I18

NOTE. — (1): ID. (2): Gas-phase metallicity. (3): Abundance ratio of $\log(\text{Fe}/\text{O})$. (4): Emission line ratio of $\log(\text{He II}/\text{H}\beta)$. (5)–(6): Emission line fluxes of $[\text{Fe III}]4658$ and $\text{He II}4686$ in the unit of $10^{-18} \text{ erg s}^{-1} \text{cm}^{-2}$. (7): Reference. I18 represents Izotov et al. (2018).

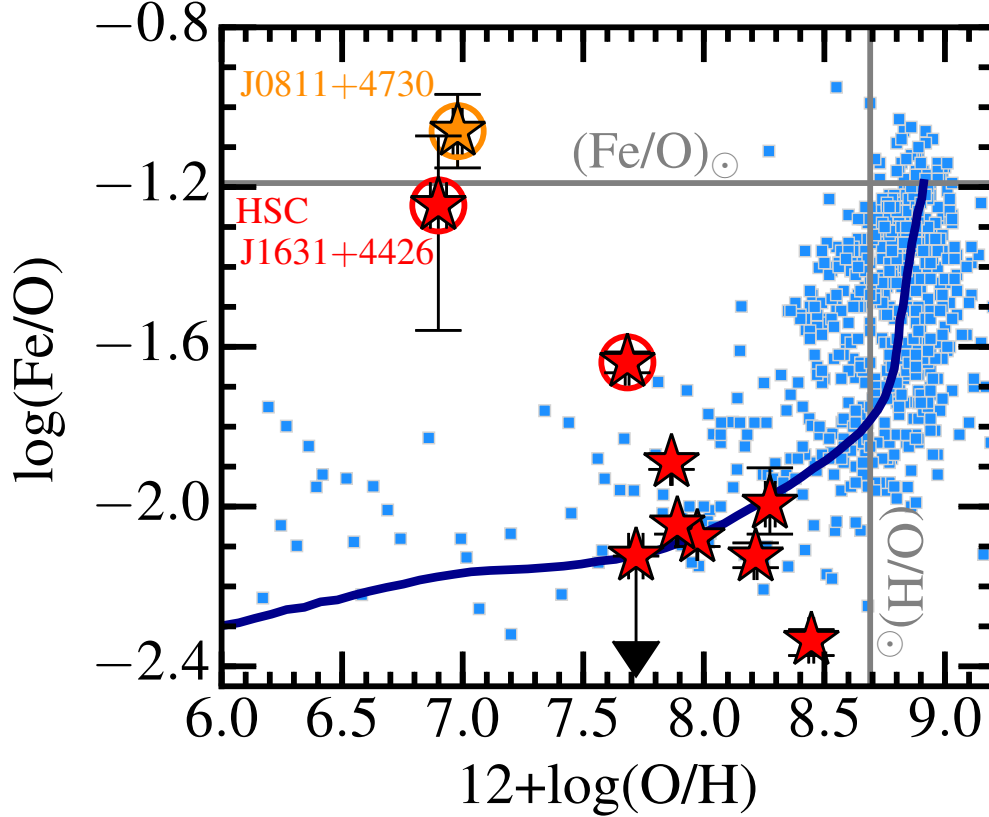


FIG. 4.— Comparison of Fe/O ratios of our metal-poor galaxies (symbols are the same as Figure 3) and Galactic stars (blue squares). We show observational data of Galactic stars from Cayrel et al. (2004), Gratton et al. (2003), and Bensby et al. (2013). Blue solid line represents a stellar Fe/O evolution model under the assumption that gas is enriched by massive stars with 9–100 M_{\odot} (Suzuki & Maeda 2018). Here we do not show HSC J2314+0154, whose T_e -metallicity and element abundances are not estimated due to the lack of the electron temperature measurement.

while the Galactic stars show the Fe/O ratio obtained from stellar atmospheric absorption lines. The nebular abundance ratios are subject to change by the effects of SNe, stellar wind, and galactic inflow in a short time scale (i.e., $\lesssim 10$ Myr). By contrast, the abundance ratios of Galactic stars (i.e., dwarf and subdwarf stars) change little across the cosmic time because the element production proceeds very slowly and the heavy elements such as oxygen and iron are produced little in low-mass stars such as dwarf and subdwarf stars. Thus, the abundance ratios of the dwarf and subdwarf stars are almost fixed at the time of the star formation, and can be regarded as tracers of the past chemical evolution. The dwarf and subdwarf stars with low metallicities of 0.01–0.1 Z_{\odot} are as old as ~ 12 Gyr (e.g., Bensby et al. 2013), which is right after the MW formation. The two EMPgS (HSC

J1631+4426 and J0811+4730), whose Fe/O ratios deviate from the Galactic stars and the Fe/O model, suggest that their Fe/O ratios have increased for some reason right after the galaxy formation. Below, we discuss three scenarios that might be able to explain the Fe/O deviation of the two EMPgS.

The first scenario is the preferential dust depletion of iron, suggested by Rodríguez & Rubin (2005) and Izotov et al. (2006). Rodríguez & Rubin (2005) and Izotov et al. (2006) discuss that gas-phase Fe/O ratios decrease as a function of metallicity in the range of $12+\log(\text{O}/\text{H}) \lesssim 8.5$ because iron elements are depleted into dust more effectively than oxygen. The depletion becomes dominant in a higher metallicity range, where the dust production becomes more efficient. For dust-free (i.e., metal-poor) galaxies, gas-phase Fe/O ratios are

expected to become comparable to the observational results of Galactic stars and the Fe/O evolution model. Although the dust depletion may explain the negative Fe/O slope, it does *not* explain the fact that the two EMPGs (HSC J1631+4426 and J0811+4730) show higher Fe/O ratios than the Galactic stars and models at fixed metallicity. In addition, as we have seen in Section 4.1 and Table 2, most of our metal-poor galaxies show $E(B-V) \sim 0$ (i.e., less dusty). At least, we do not find an evidence that galaxies with a larger metallicity show larger color excesses (i.e., dustier). This means that the Fe/O decrease of our sample is not attributed to the dust depletion. Based on these facts, we rule out the first scenario.

The second scenario is a combination of metal enrichment and gas dilution caused by inflow. In this scenario, we assume that EMPGs are formed from metal-enriched gas with the solar metallicity and solar Fe/O ratio. The Fe/O evolution models suggest that the Fe/O ratio increases at $12+\log(\text{O}/\text{H}) \gtrsim 8.0$ due to the contribution of type-Ia SNe ~ 1 Gyr after the start of the star formation. Such mature galaxies also tend to have the solar metallicity (i.e., O/H) at the same time. If primordial gas (i.e., almost metal free) falls into the metal-enriched galaxies, the metallicity (i.e., O/H) decreases while the Fe/O ratio does not change. At first glance, this scenario seems to explain the Fe/O deviation of the two EMPGs. However, if the second scenario is true, both the Fe/O and N/O ratios should match solar abundances because the N/O ratio also reaches the solar N/O ratio, $\log(\text{N}/\text{O})_{\odot} = -0.86$, at the solar metallicity (Sections 1 and 5.1.2). As we have seen in the panel (c) of Figure 3, the two deviating EMPGs, HSC J1631+4426 and J0811+4730 (encircled by a red or orange circle at $12+\log(\text{O}/\text{H}) \sim 7.0$) have a strong 2σ upper limit of <0.14 (N/O) $_{\odot}$ and a low value of 0.21 (N/O) $_{\odot}$, respectively. These low N/O ratios suggest that the two deviating EMPGs are experiencing the primary nucleosynthesis, not the secondary nucleosynthesis expected to start ~ 1 Gyr after the onset of the star formation. This also means that the high Fe/O ratios are not attributed to the type-Ia SNe, which arise ~ 1 Gyr after the onset of the star formation. This conclusion is also consistent with the fact that the two EMPGs are very young, $\lesssim 50$ Myr (Paper I). We exclude the second scenario because the second scenario does not explain the observed Fe/O and N/O ratios simultaneously.

The third scenario is the contribution of super massive stars beyond $300 M_{\odot}$. Super massive stars beyond $300 M_{\odot}$ eject much iron at the time of core-collapse SN explosion. Ohkubo et al. (2006) have calculated yields from core-collapse SNe under the assumption of the progenitor stellar mass with $500\text{--}1000 M_{\odot}$, obtaining $\sim 2\text{--}40$ (Fe/O) $_{\odot}$. In the super massive stars beyond $300 M_{\odot}$, an iron core grows until the iron core occupies more than 20 percent of the stellar mass. Although massive stars with $140\text{--}300 M_{\odot}$ undergo thermonuclear explosions triggered by pair-creation instability (PISNe, Barkat et al. 1967), super massive stars beyond $300 M_{\odot}$ are too massive to trigger PISNe and thus continue the iron core growth. The super massive stars beyond $300 M_{\odot}$ eject a large amount of iron by a jet stream from the massive iron core during the SN explosion. On the other hand, the core-collapse SNe of typical-mass stars ($10\text{--}50 M_{\odot}$) eject gas with an average of ~ 0.4 (Fe/O) $_{\odot}$ (Tominaga et al. 2007, IMF integrated in the range of $10\text{--}50 M_{\odot}$), which

is below the solar Fe/O ratio. Yields of type-Ia SNe calculated by Iwamoto et al. (1999) show ~ 40 (Fe/O) $_{\odot}$. Of the three types of SNe, only the type-Ia SNe and the SNe of super massive stars ($>300 M_{\odot}$) contribute to the iron enrichment larger than the solar Fe/O ratio. As we have discussed in the second scenario above, the low N/O ratios of the two EMPGs suggest that their high Fe/O ratios are not explained by type-Ia SNe. Ruling out the type-Ia SNe, we find that the remaining possibility is the contribution from the SNe of super massive stars beyond $300 M_{\odot}$. We also confirm that SNe of the super massive stars ($>300 M_{\odot}$) do not change N/O ratios in comparison with the core-collapse SNe of typical massive stars (Iwamoto et al. 1999; Ohkubo et al. 2006), strengthening the reliability of the super massive star ($>300 M_{\odot}$) scenario.

In summary of this subsection, we have discussed the three scenarios that might be able to explain the high Fe/O ratios of the two EMPGs (HSC J1631+4426 and J0811+4730). We suggest that the high Fe/O ratios of the two EMPGs are attributed to the contribution from core-collapse SNe of super massive stars beyond $300 M_{\odot}$. The contribution of super massive stars beyond $300 M_{\odot}$ to the iron enhancement has never been discussed by previous studies including Izotov et al. (2006) and Izotov et al. (2018). Many previous studies (e.g., Fragos et al. 2013a,b; Stanway et al. 2016; Suzuki & Maeda 2018; Xiao et al. 2018) assume the IMF maximum stellar mass (M_{max}) at $M_{\text{max}}=100$, 120, or $300 M_{\odot}$, ignoring super massive stars beyond $300 M_{\odot}$, so this paper sheds light on the super massive stars beyond $300 M_{\odot}$ in metal-poor galaxies undergoing the early-phase galaxy formation.

5.2. Ionizing Radiation

5.2.1. Emission Line Ratios

We investigate ionizing radiation of our metal-poor galaxy sample by comparing emission line ratios of various ions. Figure 5 shows four emission line ratios of [O II]3727,3729/H β , [Ar III]4740/H β , [O III]5007/H β , and [Ar IV]7136/H β as a function of metallicity. Among many emission lines detected in our spectroscopy, we choose the [O II]3727,3729, [Ar III]4740, [O III]5007, and [Ar IV]7136 emission lines for two reasons below. The first reason is that oxygen and argon are both α elements, and thus the Ar/O abundance ratio is almost constant as we confirm in Section 5.1. Thus, emission line ratios are simply interpreted by ionizing radiation intensity and/or hardness, free from variance of element abundance ratio. The second reason is that the four lines are sensitive to ionization photons in a wide energy range from 13.6 to 40.7 eV. The [O II]3727,3729, [Ar III]4740, [O III]5007, and [Ar IV]7136 lines are emitted via spontaneous emission after collisional excitation of O $^+$, Ar $^{2+}$, O $^{2+}$, and Ar $^{3+}$, respectively. Table 5 summarizes these emission line processes and corresponding photon energy required to emit these lines.

In panels of (a)–(d) of Figure 5, we show local, average SFGs of Andrews & Martini (2013, AM13 hereafter) with black circles. We regard the AM13 SFGs as local averages because the AM13 sample is obtained by the SDSS composite spectra in bins of wide SFR and stellar-mass ranges. In panels of (a)–(d), the

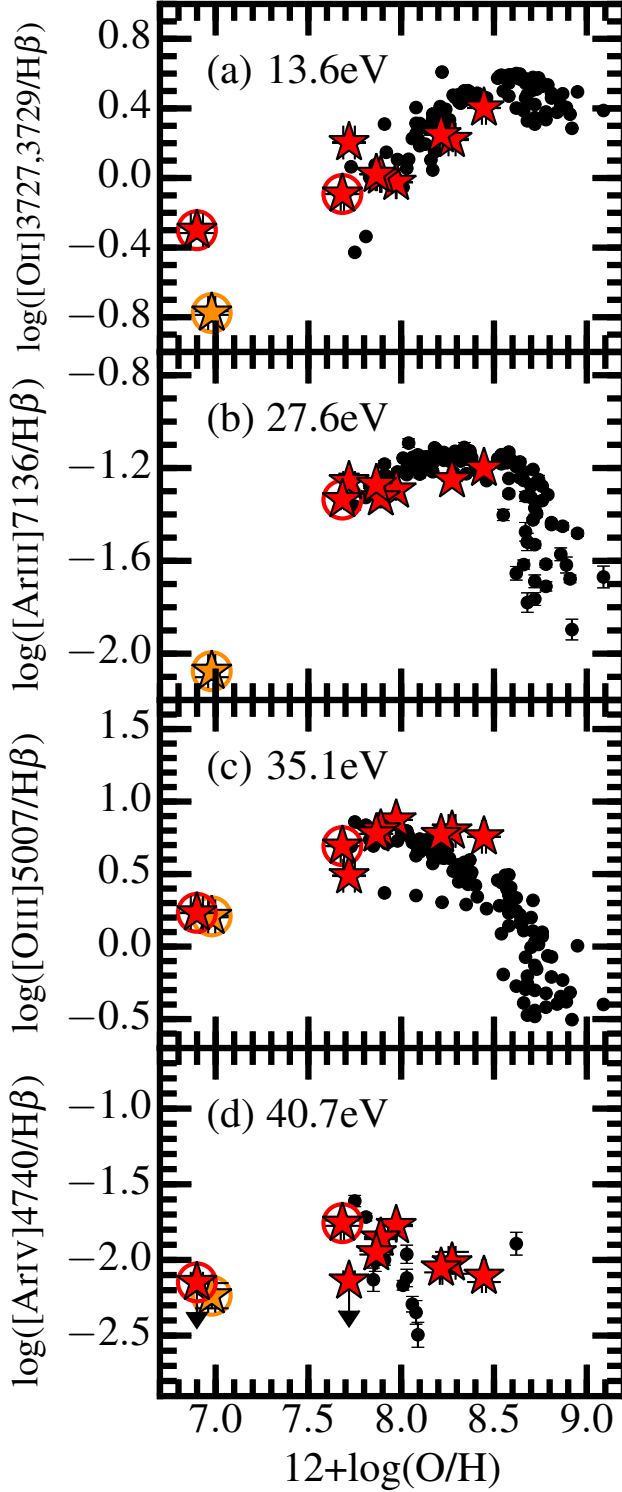


FIG. 5.— Dust-corrected emission line ratios of $[\text{O II}]3727,3729$, $[\text{Ar III}]4740$, $[\text{O III}]5007$, and $[\text{Ar IV}]7136$ to $\text{H}\beta$ in panels (a)–(d). Symbols are the same as in Figure 3. Here we do not show HSC J2314+0154 as well, whose T_e -metallicity and element abundances are not estimated. The ionization potentials of O^0 , Ar^{2+} , O^+ , and Ar^{3+} ions (13.6, 27.6, 35.1, and 40.7 eV, respectively) are presented in panels (a)–(d). Black circles represent averages of local SFGs obtained with SDSS composite spectra (Andrews & Martini 2013). We do not show galaxies whose nebular emission line is strongly affected by the sky emission line.

TABLE 5
SUMMARY OF EMISSION LINE PROCESS, IONIZATION
PROCESS AND IONIZATION POTENTIAL

Line	Emission Process	Ionization Process	Ionization Potential (eV)
$\text{H}\beta$	Re	$\text{H}^0 + \gamma \rightarrow \text{H}^+$	13.6
$[\text{O II}]3727$	CE	$\text{O}^0 + \gamma \rightarrow \text{O}^+$	13.6
$[\text{Ar III}]4740$	CE	$\text{Ar}^{2+} + \gamma \rightarrow \text{Ar}^{3+}$	27.6
$[\text{O III}]5007$	CE	$\text{O}^+ + \gamma \rightarrow \text{O}^{2+}$	35.1
$[\text{Ar IV}]7136$	CE	$\text{Ar}^{3+} + \gamma \rightarrow \text{Ar}^{4+}$	40.7
$\text{He II}4686$	Re	$\text{He}^+ + \gamma \rightarrow \text{He}^{2+}$	54.4

NOTE. — In the column of emission processes, Re and CE represent the recombination and collisional excitation.

AM13 SFGs form sequences as a function of metallicity. The sequences of $[\text{O II}]3727,3729/\text{H}\beta$ and $[\text{Ar III}]4740/\text{H}\beta$ show peaks at around $12+\log(\text{O}/\text{H}) \sim 8.7$ and 8.3 , respectively. The $[\text{O III}]5007/\text{H}\beta$ and $[\text{Ar IV}]7136/\text{H}\beta$ ratios may also have peaks around $12+\log(\text{O}/\text{H}) \sim 8.0$ and $12+\log(\text{O}/\text{H}) \sim 7.2$ – 7.7 by interpolating AM13 SFGs and our metal-poor galaxies. Recalling that the $[\text{O II}]3727,3729$, $[\text{O III}]5007$, $[\text{Ar III}]4740$, and $[\text{Ar IV}]7136$ lines are sensitive to ionizing photon above 13.6, 35.1, 27.6, and 40.7 eV, respectively, we find that the peak metallicities decrease with increasing ionizing potentials of the corresponding emission lines. The peak transition demonstrates that ISM is irradiated by more intense or harder ionizing radiation in lower metallicity, as suggested by previous studies (e.g., Nakajima & Ouchi 2014; Steidel et al. 2016; Nakajima et al. 2016; Kojima et al. 2017). We also find that our metal-poor galaxies fall on the sequences of AM13 SFGs within a scatter. Thus, we infer that our metal-poor galaxies and the AM13 SFGs have a similar spectral shape in the energy range of 13.6–40.7 eV for a given metallicity.

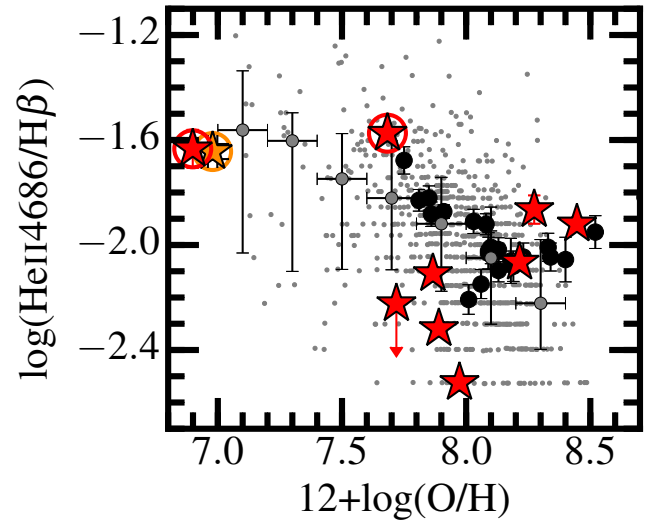


FIG. 6.— Emission line ratios of $\text{He II}4686/\text{H}\beta$ as functions of metallicity. Symbols are the same as in Figure 5. Here we do not show HSC J2314+0154, whose T_e -metallicity and element abundances are not estimated. Gray dots are individual local galaxies of S19 with an $\text{He II}4686$ detection. Gray circles and error bars show medians and 68%-percentile scatters of the S19 sample obtained in each metallicity bin, respectively.

Figure 6 shows $\text{He II}4686/\text{H}\beta$ ratios of our metal-poor galaxies as a function of metallicity, as well as the AM13 SFGs (black circles). The AM13 SFGs show almost constant $\text{He II}4686/\text{H}\beta$ ratios around $\log(\text{He II}4686/\text{H}\beta) \sim -2.0$ in the range of $12+\log(\text{O}/\text{H})=8.1-8.6$, while the $\text{He II}4686/\text{H}\beta$ ratios increase with decreasing metallicity below $12+\log(\text{O}/\text{H})=8.1$. Our metal-poor galaxies show a wide range of $\text{He II}4686/\text{H}\beta$ ratios between $\log(\text{He II}4686/\text{H}\beta) \sim -1.6$ and -2.6 . The distribution of our metal-poor galaxies are similar to those of SFGs of Schaerer et al. (2019, S19 hereafter). Among our metal-poor galaxies, three EMPGs (encircled by red and orange circles) show highest $\text{He II}4686/\text{H}\beta$ ratios around $\log(\text{He II}4686/\text{H}\beta) \sim -1.6$, including the two representative EMPGs, HSC J1631+4426 and J0811+4730 (Izotov et al. 2018).

5.2.2. Strong $\text{He II}4686$ Line

As described in Section 1, the physical mechanism of the $\text{He II}4686$ emission from SFGs is still under debate. S19 aim to explain the $\text{He II}4686$ emission from local SFGs with high mass X-ray binary (HMXB) models of Fragos et al. (2013a,b). HMXBs are binary systems consisting of a compact object (such as BH) and a companion star. The companion star provides gas onto the compact object, and creates a hot accretion disk around the compact object. The hot accretion disk radiates very hard, power-law radiation ranging from UV to X-ray. Fragos et al. (2013a,b) carefully calculate the HMXB evolution along the star-formation history, and predict total X-ray luminosities (L_X) from a galaxy as functions of metallicity and age. S19 convert an L_X/SFR ratio to the $\text{He II}4686/\text{H}\beta$ ratio, under the simple assumptions of $\text{He II}4686/\text{H}\beta=1.74 \times Q(\text{He}^+)/Q(\text{H})$ (Case B recombination of 20,000K, Stasińska et al. 2015), $Q(\text{H})/\text{SFR}=9.26 \times 10^{52} \text{ photons s}^{-1}/(M_\odot \text{ yr}^{-1})$ (Kennicutt 1998), and hardness of $Q(\text{He}^+)/L_X=2 \times 10^{10} \text{ photon erg}^{-1}$. Here, the $Q(\text{He}^+)$ and $Q(\text{H})$ are defined by ionizing photon production rates above 54.4 and 13.6 eV, respectively. S19 also use the BPASS binary stellar synthesis models of Xiao et al. (2018) to associate stellar ages with $\text{EW}_0(\text{H}\beta)$.

Figure 7 compares $\text{He II}4686/\text{H}\beta$ ratios of our metal-poor galaxies and those obtained by the S19 HMXB models (solid lines) as a function of $\text{EW}_0(\text{H}\beta)$. The solid lines trace time evolution of $\text{He II}4686/\text{H}\beta$ and $\text{EW}_0(\text{H}\beta)$ with different metallicities of 0.05, 0.10, 0.20, and 0.50 Z_\odot . The $\text{EW}_0(\text{H}\beta)$ decreases and the $\text{He II}4686/\text{H}\beta$ ratio increases as time passes due to the stellar evolution and HMXB evolution, respectively. The HMXB models (especially 0.05 and 0.10 Z_\odot) show a rapid increase of $\text{He II}4686/\text{H}\beta$ around $\text{EW}_0(\text{H}\beta) \sim 100-300 \text{ \AA}$. The $\text{EW}_0(\text{H}\beta) \sim 100-300 \text{ \AA}$ corresponds to $\sim 5 \text{ Myr}$ in the BPASS binary stellar synthesis models. The rapid increase is triggered by the first compact object formation (i.e., the first HMXB formation) after $\sim 5 \text{ Myr}$ of the starburst. As shown in Figure 7, the HMXB models of S19 have quantitatively explained the $\text{He II}4686/\text{H}\beta$ ratios of half of our metal-poor galaxies. However, we find that the other five metal-poor galaxies are not explained by the HMXB model, which fall in the ranges of $\text{EW}_0(\text{H}\beta) > 100 \text{ \AA}$ and $\log(\text{He II}4686/\text{H}\beta) > -2.0$. Interestingly, three out

of the five metal-poor galaxies are EMPGs (i.e., $Z < 0.1 Z_\odot$), which are marked with red and orange circles in Figure 7. Especially, HSC J1631+4426 (0.016 Z_\odot) and J0811+4730 (0.019 Z_\odot) are the representative EMPGs with the two lowest metallicities reported to date, showing high $\text{He II}4686/\text{H}\beta$ ratios of $\log(\text{He II}4686/\text{H}\beta) \sim -1.6$. Furthermore, the S19 SFG sample also include galaxies in the same ranges of $\text{EW}_0(\text{H}\beta) > 100 \text{ \AA}$ and $\log(\text{He II}4686/\text{H}\beta) > -2.0$. S19 have argued that other X-ray sources are likely to appear fairly soon after the onset of the star formation ($\lesssim 5 \text{ Myr}$) in galaxies with high values of $\text{EW}_0(\text{H}\beta)$ and $\text{He II}4686/\text{H}\beta$. Although Wolf-Rayet (WR) stars might contribute to the strong $\text{He II}4686$ emission, we do not find broad $\text{He II}4686$ emission lines typical of the WR stars (Brinchmann et al. 2008; López-Sánchez & Esteban 2009) in our spectra. Instead, S19 suggest that an underlying older population or shocks could also contribute to the high $\text{He II}4686/\text{H}\beta$ ratios.

In addition to the S19 suggestions, we propose two other possibilities, for the first time, which can explain the high $\text{He II}4686/\text{H}\beta$ ratios seen in the range of $\text{EW}_0(\text{H}\beta) > 100 \text{ \AA}$. First, we propose a possibility of super massive stars beyond $300 M_\odot$. The HMXB models of Fragos et al. (2013a,b) assume the Kroupa IMF (Kroupa 2001; Kroupa & Weidner 2003) with the maximum stellar mass of $M_{\text{max}}=120 M_\odot$. Thus, in the HMXB models of (Fragos et al. 2013a,b), the first HMXBs emerge $\sim 5 \text{ Myr}$ after the start of the star formation, which corresponds to a lifetime of a star with $120 M_\odot$. On the other hand, stars more massive than $120 M_\odot$ are expected to have a shorter life time than stars with $120 M_\odot$. According to the theoretical study of Yungelson et al. (2008), super massive stars with $300 M_\odot$ and $1000 M_\odot$ die after 2.5 and 2.0 Myr after the onset of the star formation, respectively. As described in Section 5.1.3, stars between 140 and $300 M_\odot$ undergo thermonuclear explosions triggered by PISNe (Barkat et al. 1967), and do not leave any compact object (e.g., Heger & Woosley 2002). On the other hand, stars beyond $300 M_\odot$ experience core-collapse SNe and form intermediate-mass BHs (IMBH, e.g., Ohkubo et al. 2006). Ohkubo et al. (2006) estimate that BH masses become ~ 230 and $\sim 500 M_\odot$ for stars with initial masses of 500 and $1000 M_\odot$, respectively. Thus, when we assume super massive stars beyond $300 M_\odot$, IMBHs appear as early as $\sim 2 \text{ Myr}$, and part of the IMBHs may form HMXBs. Accretion disks of IMBHs emit very hard radiation including ionizing photons above 54.4 eV, which boosts the $\text{He II}4686$ intensity. A galaxy as young as $\sim 2 \text{ Myr}$ has $\text{EW}_0(\text{H}\beta) \sim 300-400 \text{ \AA}$ according to the BPASS models. Under the assumption of super massive stars beyond $300 M_\odot$, the $\text{He II}4686/\text{H}\beta$ ratio is expected to start increasing at around $\text{EW}_0(\text{H}\beta) \sim 300-400 \text{ \AA}$. Such a model may cover the regions of $\text{EW}_0(\text{H}\beta) > 100 \text{ \AA}$ and $\log(\text{He II}4686/\text{H}\beta) > -2.0$ shown in Figure 7. Thus, we suggest that super massive stars beyond $300 M_\odot$ would be able to explain the high ratios, $\log(\text{He II}4686/\text{H}\beta) > -2.0$ in the galaxies with $\text{EW}_0(\text{H}\beta) > 100 \text{ \AA}$. Note again that galaxies with $\log(\text{He II}4686/\text{H}\beta) > -2.0$ and $\text{EW}_0(\text{H}\beta) > 100 \text{ \AA}$ includes EMPGs, HSC J1631+4426 SDSS J2115-1734, and J0811+4730. These EMPGs might form super mas-

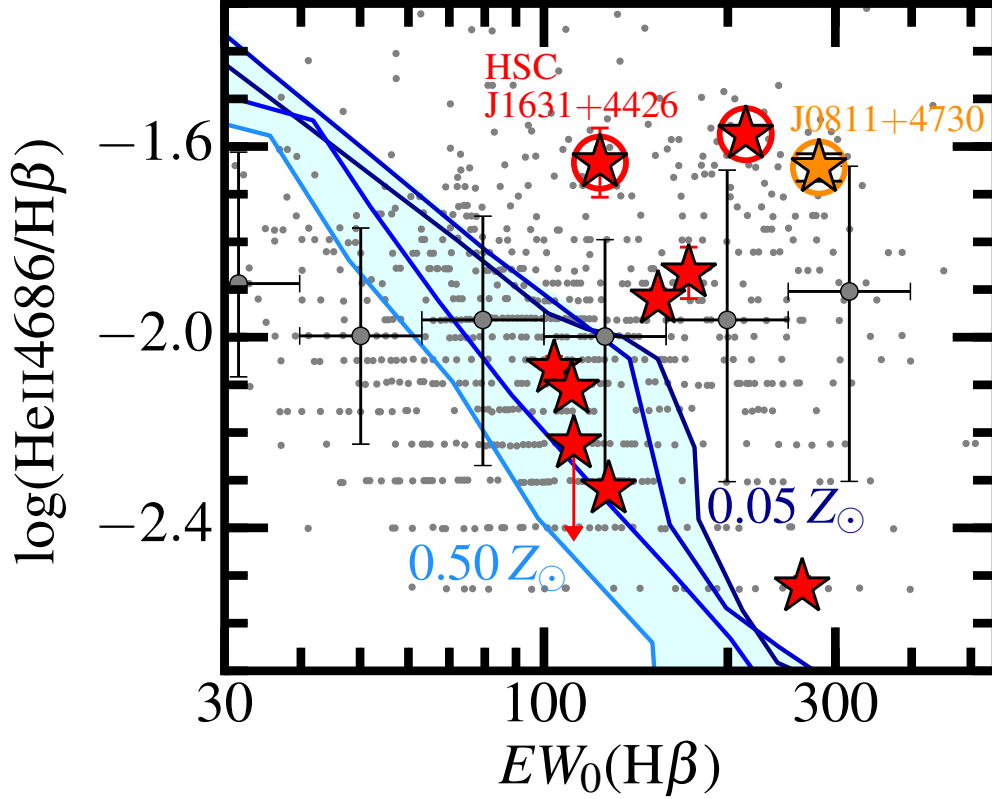


FIG. 7.— Same as Figure 6, but as a function of H β equivalent width, $EW_0(H\beta)$. Symbols are the same as in Figures 5 and 6. Here we do not show HSC J2314+0154, whose T_e -metallicity and element abundances are not estimated. Solid lines represent the S19 HMXB models, tracing time evolution of He II 4686/H β and $EW_0(H\beta)$ with different metallicities of 0.05, 0.10, 0.20, and 0.50 Z_\odot (from dark blue to light blue).

sive star beyond $300 M_\odot$ from their extremely metal-poor gas. However, our explanation and the interpretation of S19 are based on some simple assumptions that associate the HMXB models and the BPASS stellar synthesis models. We propose to construct self-consistent SED models ranging from X-ray to UV with the HMXB evolution models under the assumption of $M_{\max} > 300 M_\odot$.

Second, we also suggest a possibility of a metal-poor AGN, which can contribute to boost the He II 4686 intensity of the very young galaxies. In Paper I, we have confirmed that all of our metal-poor galaxies fall on the SFG region of the BPT diagram defined by the maximum photoionization models with stellar radiation (Kewley et al. 2001). However, Kewley et al. (2013) suggest that emission-line ratios calculated under the assumption of a metal-poor AGN also fall on the SFG region. Thus, we cannot exclude the possibility of a metal-poor AGN. Groves et al. (2004a,b) have constructed the photo-ionization models under the assumption of AGN-like, power-law radiation. The models of Groves et al. (2004a,b) predict very strong He II 4686 emission represented by $\log(\text{He II } 4686/\text{H}\beta) \sim -1.5$ to 0.0 . On the other hand, photo-ionization models with stellar radiation (Xiao et al. 2018) predict $\log(\text{He II } 4686/\text{H}\beta) \lesssim -2.5$. To explain the observed ratios of $\log(\text{He II } 4686/\text{H}\beta) \sim -2.0$, the combination of AGN and stellar radiation is required. We have checked the archival data of ROSAT and XMM, and found no detection in X-ray. This is because the data are ~ 2 orders of magnitudes shallower than expected X-

ray luminosities ($\sim 10^{-14} \text{ erg s}^{-1} \text{ cm}^{-2}$) of our metal-poor galaxy sample, which are obtained under the assumption of $L_{2\text{keV}}-M_{\text{UV}}$ relation of AGN (Lusso et al. 2010). Deep X-ray observations are required to constrain X-ray sources of metal-poor galaxies.

5.3. Formation Mechanism of Super Massive Stars beyond $300 M_\odot$

Below, we focus only on the two representative EMPGs, HSC J1631+4426 ($0.016 Z_\odot$) and J0811+4730 ($0.019 Z_\odot$) and discuss their high Fe/O ratios and He II 4686/H β ratios. The two representative EMPGs, HSC J1631+4426 and J0811+4730 show the two lowest metallicities reported to date. In Section 5.1.3, we have found that the two EMPGs, HSC J1631+4426 and J0811+4730 show Fe/O ratios ~ 1.0 dex higher than Galactic stars and the Fe/O evolution models at fixed metallicity. We have concluded that the high Fe/O ratios are explained by core-collapse SNe of super massive stars beyond $300 M_\odot$. In Section 5.2.2, we have also found that the two EMPGs, HSC J1631+4426 and J0811+4730, show both high He II 4686/H β ratios ($\sim 1/40$) and high $EW_0(H\beta)$ ($\sim 100\text{--}300 \text{ \AA}$). We have suggested that IMBH formed from super massive stars beyond $300 M_\odot$ can explain the high He II 4686/H β ratios. Interestingly, the scenario of super massive stars beyond $300 M_\odot$ explains both the high Fe/O ratios and the high He II 4686/H β ratios of our EMPGs with the low metallicities ($\sim 0.02 Z_\odot$), young ages ($\lesssim 50 \text{ Myr}$), and very low stellar mass

($\sim 10^5\text{--}10^6 M_\odot$), which are undergoing an early stage of the galaxy formation.

The idea of super massive stars beyond $300 M_\odot$ is not necessarily extraordinary. Crowther et al. (2010, 2016) have claimed the spectroscopic identification of super massive stars with $\sim 320 M_\odot$ in the R136 star cluster of Large Magellanic Cloud (LMC). The identification of an IMBH with $M_{\text{BH}} > 700 M_\odot$ in a star cluster of M82 (Matsumoto et al. 2001; Ebisuzaki et al. 2001; Kaaret et al. 2001) is another indirect trace of a super massive star beyond $300 M_\odot$. This is because the SN numerical simulation (Ohkubo et al. 2006) suggests that a star with initial masses beyond $300 M_\odot$ leaves an IMBH with $\gtrsim 100 M_\odot$.

We may wonder how such super massive stars are formed. Below, we discuss the formation mechanisms of super massive stars beyond $300 M_\odot$. Theoretical studies (e.g., Bromm & Loeb 2004; Omukai & Palla 2003) suggest that metal-free (pop-III) stars are typically super massive ($> 300 M_\odot$) because gas cooling becomes insufficient and the fragmentation mass becomes large in metal-free gas. The critical metallicity (Z_{crit}), below which super massive stars can be formed directly, is $Z_{\text{crit}} \sim 10^{-6}$ to $10^{-4} Z_\odot$, theoretically (e.g., Bromm et al. 2001; Santoro & Shull 2006; Schneider et al. 2006; Smith & Sigurdsson 2007). The critical metallicity ($Z_{\text{crit}} \sim 10^{-6}\text{--}10^{-4} Z_\odot$) is much lower than our metallicity measurements of our EMPGs, $\sim 0.02 Z_\odot$. Thus, the direct gas collapse is unlikely to be the formation mechanism of the super massive stars beyond $300 M_\odot$ in our EMPGs.

We briefly discuss another possibility that EMPGs previously had a metallicity near the critical metallicity ($\sim 10^{-6}\text{--}10^{-4} Z_\odot$) at the time of the galaxy formation, and the metallicity has been increased by SNe within a short period. The metallicity at the time of the galaxy formation namely depends on the metallicity of the inflow gas, which may come from a void region free from the metal contamination. Based on the observational results of metal-poor galaxies, Thuan et al. (2005) speculate that the metallicity lower limit (so-called “metallicity floor”) might exist at $\sim 10^{-2} Z_\odot$ at $z = 0$ because the IGM has slightly been metal-enriched by the past star formation activities even in the void regions. In addition, observational studies of Lyman alpha absorption systems (e.g., Prochaska et al. 2003; Rafelski et al. 2012; Lehner et al. 2013; Quiret et al. 2016) have not yet discovered Lyman alpha absorption system below $\sim 10^{-2} Z_\odot$ at $z = 0\text{--}1$. Hydrodynamical simulation of Martizzi et al. (2019) also demonstrates that the average IGM metallicity in the void region is $\sim 10^{-2} Z_\odot$ at $z = 0$. We do not necessarily remove the possibility that EMPGs had a metallicity near the critical metallicity ($\sim 10^{-6}\text{--}10^{-4} Z_\odot$) at the time of the galaxy formation because part of the IGM would reach below $\sim 10^{-2} Z_\odot$ (Hafen et al. 2017) due to a metallicity fluctuation. However, the direct gas collapse may not be, at least, the main formation mechanism of the super massive stars beyond $300 M_\odot$.

Ebisuzaki et al. (2001) and Portegies Zwart et al. (1999, 2004, 2006) has presented another formation mechanism of super massive stars beyond $300 M_\odot$, where super massive stars are formed by stellar mergers under

the very dense condition in a star cluster. Numerical simulations suggest that super massive stars of $800\text{--}3000 M_\odot$ have been formed by stellar mergers within ~ 3 Myr (Portegies Zwart et al. 2004). The super massive star formation mechanism of Portegies Zwart et al. (2004) is presented to explain an IMBH discovered in a star cluster of M82 (Matsumoto et al. 2001; Ebisuzaki et al. 2001; Kaaret et al. 2001). The estimated BH mass of the M82 IMBH is $M_{\text{BH}} > 700 M_\odot$. This stellar merger mechanism requires the very dense star forming regions, which are typical in young, metal-poor galaxies. Indeed, our sample EMPGs are undergoing the intensive star-formation represented by high sSFRs ($\sim 300 \text{ Gyr}^{-1}$, Kojima et al. 2019) and small sizes (~ 100 pc, Paper III). Although the stellar merger mechanism *itself* does not depend on metallicity, the formation mechanism of the very dense star forming regions may depend on metallicity. A possible scenario is that a large amount of massive stars are formed within a compact region by a primordial gas (i.e., almost metal free) infall from the inter-galactic space (KS1-EMPG in Paper III). This scenario may be associated with the top heavy IMF.

In this paper, we find that two representative EMPGs ($\sim 0.02 Z_\odot$) show both the high Fe/O ratios and the high He II4686/H β ratios, which are not explained by the previous models assuming massive stars up to 100 or $120 M_\odot$. In the end of this section, we summarize one possible picture that we have suggested in each section of this paper. In our picture, EMPGs are formed by a primordial gas infall, which also forms star clusters with a very high number density of massive stars (Paper III). In such very dense regions of star clusters, stellar mergers trigger the formation of super massive stars beyond $300 M_\odot$ within ~ 3 Myr (Portegies Zwart et al. 2004). The super massive stars beyond $300 M_\odot$ eventually eject much iron through the core-collapse SNe in ~ 2 Myr (Ohkubo et al. 2006; Yungelson et al. 2008) and form IMBHs ($M_{\text{BH}} \gtrsim 100 M_\odot$, Ohkubo et al. 2006) boosting the He II4686 emission. To testify this picture, spectroscopic observations are required with a high spacial resolution in multi-wavelength to identify the formation mechanism of EMPGs and to directly detect IMBH signatures in EMPGs.

6. SUMMARY

We investigate element abundance ratios and ionizing radiation of 10 metal-poor galaxies at $z \lesssim 0.03$, which have been discovered in the wide-field imaging data of Subaru/Hyper Prime-Cam (HSC) and Sloan Digital Sky Survey (SDSS) by Kojima et al. (2019). The 10 metal-poor galaxies are represented by low metallicities, $12+\log(\text{O}/\text{H}) = 6.90\text{--}8.45$, low stellar masses, $\log(M_\star/M_\odot) = 4.95\text{--}7.06$, and high specific star-formation rates ($\text{sSFR} \sim 300 \text{ Gyr}^{-1}$). These galaxies have very low masses of $\log(M_\star/M_\odot) \lesssim 6$, which are comparable to those of star clusters. Such cluster-like galaxies are undergoing the first stage of the galaxy formation. Especially, three out of the 10 galaxies are extremely metal-poor galaxies (EMPGs) defined by $12+\log(\text{O}/\text{H}) < 7.69$, including HSC J1631+4426 with the lowest metallicity ($0.016 Z_\odot$) reported to date. In addition to the 10 metal-poor galaxies, we include another EMPG from the literature (J0811+4730, Izotov et al. 2018) in the sample of this paper. J0811+4730 has the second lowest metallic-

ity of $0.019 Z_{\odot}$ reported to date. The two EMPGs (HSC J1631+4426 and J0811+4730) are key in this paper.

- We estimate element abundance ratios of Ne/O, Ar/O, and N/O of our metal-poor galaxies, and compare them with local SFGs. We find that α -element ratios of Ne/O and Ar/O show almost constant values of $\log(\text{Ne}/\text{O}) \sim -0.8$ and $\log(\text{Ar}/\text{O}) \sim -2.5$ as a function of metallicity, respectively. These constant Ne/O and Ar/O values are consistent with those of local SFGs. Most of our metal-poor galaxies have N/O ratios of $\log(\text{N}/\text{O}) \lesssim -1.5$, suggesting that our metal-poor galaxies are undergoing the primary nucleosynthesis of nitrogen due to their low metallicity and young stellar population.
- We also estimate Fe/O ratios of our metal-poor galaxies, and compare them with local SFGs. Our metal-poor galaxy sample shows a decreasing Fe/O trend with increasing metallicity, which is consistent with the previous results of local SFGs. We find that two EMPGs, HSC J1631+4426 ($0.016 Z_{\odot}$) and J0811+4730 ($0.019 Z_{\odot}$, Izotov et al. 2018), show higher Fe/O ratios than observational results of Galactic stars and a model calculation of the Fe/O evolution at fixed metallicity. Especially, HSC J1631+4426 and J0811+4730 show the solar Fe/O ratios in spite of its very low metallicity, 0.016 and $0.019 Z_{\odot}$, respectively. We discuss the three scenarios that might be able to explain the high Fe/O ratios with the extremely low metallicity: (1) the preferential dust depletion of iron, (2) a combination of metal enrichment and gas dilution caused by inflow, and (3) super massive stars beyond $300 M_{\odot}$. The scenario (1) is ruled out because the solar Fe/O ratios are not achieved by the dust depletion, and we do not see any correlation between the dust extinction and the Fe/O ratios. We also exclude the scenario (2) because the observed N/O ratios are lower than the expected solar N/O ratio when the scenario (2) is true. Thus, we conclude that the high Fe/O ratios of the two EMPGs are attributed to super massive stars beyond $300 M_{\odot}$, which is consistent with the young stellar ages of EMPGs ($\lesssim 50$ Myr).
- To probe ionizing radiation in our metal-poor galaxies, we inspect emission lines from various ions covering a wide range of ionization potentials. We choose $\text{H}\beta$, $[\text{O II}]3727, 3729$, $[\text{Ar III}]4740$, $[\text{O III}]5007$, and $[\text{Ar IV}]7136$ lines, which are sensitive to ionizing photon above 13.6, 13.6, 27.6, 35.1, and 40.7 eV, respectively. Our metal-poor galaxies and local, average SFGs show sequences of $[\text{O II}]3727, 3729/\text{H}\beta$, $[\text{Ar III}]4740/\text{H}\beta$, $[\text{O III}]5007/\text{H}\beta$, and $[\text{Ar IV}]7136/\text{H}\beta$ as a function of metallicity, and match each other within small scatters. The match between the two samples suggests that our metal-poor galaxies and local, average SFGs have a similar spectral shape in the energy range of 13.6–40.7 eV for a given metallicity.
- We find that five metal-poor galaxies show both

high $\text{He II}4686/\text{H}\beta$ ratios ($>1/100$) and high $\text{EW}_0(\text{H}\beta)$ ($>100 \text{ \AA}$). Interestingly, two out of the five metal-poor galaxies are the representative EMPGs, HSC J1631+4426 ($0.016 Z_{\odot}$) and J0811+4730 ($0.019 Z_{\odot}$). These high $\text{He II}4686/\text{H}\beta$ ratios and high $\text{EW}_0(\text{H}\beta)$ are not explained by the latest binary population stellar synthesis model and the latest HMXB model, where a maximum stellar mass cut, $120 M_{\odot}$ is used. We suggest that super massive stars beyond $300 M_{\odot}$ can explain the high $\text{He II}4686/\text{H}\beta$ ratios for galaxies of $\text{EW}_0(\text{H}\beta) > 100 \text{ \AA}$ (i.e., $\lesssim 5$ Myr). Super massive stars beyond $300 M_{\odot}$ have very short lifetimes of ~ 2 Myr, and form intermediate-mass black holes (IMBHs) of $\gtrsim 100 M_{\odot}$ as early as ~ 2 Myr after the onset of the star formation. We do not rule out a possibility of a metal-poor AGN, which can contribute to the $\text{He II}4686$ boost of the very young galaxies even at $\lesssim 5$ Myr.

- Interestingly, the scenario of super massive stars beyond $300 M_{\odot}$ explains both the high Fe/O ratios and the high $\text{He II}4686/\text{H}\beta$ ratios of our EMPGs. We also discuss a formation mechanism of super massive stars beyond $300 M_{\odot}$. The direct collapse of metal-poor gas is unlikely to be the formation mechanism because the critical metallicity ($Z_{\text{crit}} \sim 10^{-6} - 10^{-4} Z_{\odot}$), below which super massive stars can be formed directly, is much lower than the metallicities of the two representative EMPGs, $\sim 0.02 Z_{\odot}$. Instead, super massive stars beyond $300 M_{\odot}$ would be formed by stellar mergers under the very dense condition in a star cluster. In this picture, EMPGs are formed by a primordial gas inflow, which also forms star clusters with a very high number density of massive stars. In such very dense regions, stellar mergers trigger the formation of super massive stars beyond $300 M_{\odot}$ within ~ 3 Myr. The super massive stars beyond $300 M_{\odot}$ eventually eject much iron through the core-collapse SNe in ~ 2 Myr and form IMBHs ($M_{\text{BH}} \gtrsim 100 M_{\odot}$) boosting the $\text{He II}4686$ emission.

We are grateful to Lennox Cowie, Akio Inoue, Taddy Kodama, Matthew Malkan, and Daniel Stark for their important and useful comments. We thank John David Silverman and Anne Verhamme for their helpful comments on our survey name. We would like to express our special thanks to Daniel Kelson for his great efforts in helping us reduce and calibrate our MagE data. We are also grateful to Yuri Izotov for his permission to show a spectrum of a representative EMPG (J0811+4730) in this paper so that we can compare it with our galaxy spectra.

We also thank staffs of the Las Campanas observatories, the Subaru telescope, and the Keck observatories for helping us with our observations. The observations were carried out within the framework of Subaru-Keck time exchange program, where the travel expense was supported by the Subaru Telescope, which is operated by the National Astronomical Observatory of Japan. The

authors wish to recognize and acknowledge the very significant cultural role and reverence that the summit of Maunakea has always had within the indigenous Hawaiian community. We are most fortunate to have the opportunity to conduct observations from this mountain.

The Hyper Suprime-Cam (HSC) collaboration includes the astronomical communities of Japan and Taiwan, and Princeton University. The HSC instrumentation and software were developed by the National Astronomical Observatory of Japan (NAOJ), the Kavli Institute for the Physics and Mathematics of the Universe (Kavli IPMU), the University of Tokyo, the High Energy Accelerator Research Organization (KEK), the Academia Sinica Institute for Astronomy and Astrophysics in Taiwan (ASIAA), and Princeton University. Funding was contributed by the FIRST program from the Japanese Cabinet Office, the Ministry of Education, Culture, Sports, Science and Technology (MEXT), the Japan Society for the Promotion of Science (JSPS), Japan Science and Technology Agency (JST), the Toray Science Foundation, NAOJ, Kavli IPMU, KEK, ASIAA, and Princeton University.

This paper makes use of software developed for the Large Synoptic Survey Telescope. We thank the LSST Project for making their code available as free software at <http://dm.lsst.org>.

This paper is based on data collected at the Subaru Telescope and retrieved from the HSC data archive system, which is operated by Subaru Telescope and Astronomy Data Center (ADC) at NAOJ. Data analysis was in part carried out with the cooperation of Center for Computational Astrophysics (CfCA), NAOJ.

The Pan-STARRS1 Surveys (PS1) and the PS1 public science archive have been made possible through contributions by the Institute for Astronomy, the University of Hawaii, the Pan-STARRS Project Office, the Max Planck Society and its participating institutes, the Max Planck Institute for Astronomy, Heidelberg, and the Max Planck Institute for Extraterrestrial Physics, Garching, The Johns Hopkins University, Durham University, the University of Edinburgh, the Queens University Belfast, the Harvard-Smithsonian Center for Astrophysics, the Las Cumbres Observatory Global Telescope Network Incorporated, the National Central University of Taiwan, the Space Telescope Science Institute, the National Aeronautics and Space Administration under grant No. NNX08AR22G issued through the Planetary Science Division of the NASA Science Mission Directorate, the National Science Foundation grant No. AST-1238877, the University of Maryland, Eotvos Lorand University (ELTE), the Los Alamos National Laboratory, and the Gordon and Betty Moore Foundation.

This work is supported by World Premier International Research Center Initiative (WPI Initiative), MEXT, Japan, as well as KAKENHI Grant-in-Aid for Scientific Research (A) (15H02064, 17H01110, and 17H01114) through Japan Society for the Promotion of Science (JSPS). T.K., K.Y., Y.S., and M. Onodera are supported by JSPS KAKENHI Grant Numbers, 18J12840, 18K13578, 18J12727, and 17K14257. S.F. acknowledges support from the European Research Council (ERC) Consolidator Grant funding scheme (project ConTEst, grant No. 648179). The Cosmic Dawn Center is funded by the Danish National Research Foundation under grant No. 140.

REFERENCES

- Aihara, H., Arimoto, N., Armstrong, R., et al. 2018, *PASJ*, 70, 1
Aihara, H., AlSayyad, Y., Ando, M., et al. 2019, *PASJ*, 71, 114
Albareti, F. D., Prieto, C. A., Almeida, A., et al. 2017, *ApJS*, 233, 25
Andrews, B. H., & Martini, P. 2013, *ApJ*, 765, 140
Asplund, M., Grevesse, N., Sauval, A. J., & Scott, P. 2009, *Astrophysics and Space Science*, 328, 179
Axelrod, T., Kantor, J., Lupton, R. H., & Pierfederici, F. 2010, *Proc. SPIE*, 7740, 774015
Barkat, Z., Rakavy, G., & Sack, N. 1967, *PRL*, 18, 379
Bensby, T., & Feltzing, S. 2006, *MNRAS*, 367, 1181
Bensby, T., Yee, J. C., Feltzing, S., et al. 2013, *A&A*, 549, A147
Bosch, J., Armstrong, R., Bickerton, S., et al. 2018, *PASJ*, 70, 1
Brinchmann, J., Kunth, D., & Durret, F. 2008, *A&A*, 485, 657
Bromm, V., Ferrara, A., Coppi, P., & Larson, R. 2001, *MNRAS*, 328, 969
Bromm, V., & Loeb, A. 2004, *New Astronomy*, 9, 353
Campbell, A., Terlevich, R., & Melnick, J. 1986, *MNRAS*, 223, 811
Cardelli, J. A., Clayton, G. C., & Mathis, J. S. 1989, *ApJ*, 345, 245
Cayrel, R., Depagne, E., Spite, M., et al. 2004, *A&A*, 416, 1117
Chon, S., & Omukai, K. 2020, *MNRAS*, 494, 2851
Christensen, L., Laursen, P., Richard, J., et al. 2012a, *MNRAS*, 427, 1973
Christensen, L., Richard, J., Hjorth, J., et al. 2012b, *MNRAS*, 427, 1953
Coupon, J., Czakon, N., Bosch, J., et al. 2018, *PASJ*, 70, 1
Crowther, P. A., Schnurr, O., Hirschi, R., et al. 2010, *MNRAS*, 408, 731
Crowther, P. A., Caballero-Nieves, S. M., Bostroem, K. A., et al. 2016, *MNRAS*, 458, 624
Ebisuzaki, T., Makino, J., Tsuru, T. G., et al. 2001, *ApJ*, 562, L19
Eldridge, J. J., Stanway, E. R., Xiao, L., et al. 2017, *PASA*, 34, e058
Ferland, G. J., Porter, R. L., Van Hoof, P. A. M., et al. 2013, *RMxAA*, 49, 137
Fragos, T., Lehmer, B. D., Naoz, S., Zezas, A., & Basu-Zych, A. 2013a, *ApJL*, 776, L31
Fragos, T., Lehmer, B., Tremmel, M., et al. 2013b, *ApJ*, 764, 41
Furusawa, H., Koike, M., Takata, T., et al. 2018, *PASJ*, 70, 1
Garrett, D. R. 1992, *AJ*, 103, 1330
Gratton, R. G., Carretta, E., Claudi, R., Lucatello, S., & Barbieri, M. 2003, *A&A*, 404, 187
Groves, B. A., Dopita, M. A., & Sutherland, R. S. 2004a, *ApJS*, 153, 9
—. 2004b, *ApJS*, 153, 75
Guseva, N. G., Izotov, Y. I., Fricke, K. J., & Henkel, C. 2017, *A&A*, 599, A65
Hafen, Z., Faucher-Giguère, C.-A., Anglés-Alcázar, D., et al. 2017, *MNRAS*, 469, 2292
Hanuschik, R. W. 2003, *A&A*, 407, 1157
Heger, A., & Woosley, S. E. 2002, *ApJ*, 567, 532
Isobe, Y., Ouchi, M., Kojima, T., et al. 2020, *arXiv:2004.11444*
Ivezić, Ž., Kahn, S. M., Tyson, J. A., et al. 2019a, *ApJ*, 873, 111
—. 2019b, *ApJ*, 873, 111
Iwamoto, K., Brachwitz, F., Nomoto, K., et al. 1999, *ApJS*, 125, 439
Izotov, Y. I., Guseva, N. G., Fricke, K. J., & Papaderos, P. 2009, *A&A*, 503, 61
Izotov, Y. I., Stasińska, G., Meynet, G., Guseva, N. G., & Thuan, T. X. 2006, *A&A*, 448, 955
Izotov, Y. I., & Thuan, T. X. 1998, *ApJ*, 497, 227
Izotov, Y. I., Thuan, T. X., & Guseva, N. G. 2012, *A&A*, 546, A122
—. 2019, *MNRAS*, 483, 5491
Izotov, Y. I., Thuan, T. X., Guseva, N. G., & Liss, S. E. 2018, *MNRAS*, 473, 1956
Jurić, M., Kantor, J., Lim, K.-T., et al. 2015, *arXiv e-prints*, *arXiv:1512.07914*
Kaaret, P., Prestwich, A. H., Zezas, A., et al. 2001, *MNRAS*, 321, L29
Kawanomoto, S., Uruguchi, F., Komiyama, Y., et al. 2018, *PASJ*, 70, 1
Kelson, D. 2003, *PASP*, 115, 688
Kelson, D. D., Illingworth, G. D., van Dokkum, P. G., & Franx, M. 2000, *ApJ*, 531, 159

- Kennicutt, R. C. 1998, *ARA&A*, 36, 189
- Kewley, L. J., Dopita, M. A., Leitherer, C., et al. 2013, *ApJ*, 774, 100
- Kewley, L. J., Dopita, M. A., Sutherland, R. S., Heisler, C. A., & Trevena, J. 2001, *ApJ*, 556, 121
- Kojima, T., Ouchi, M., Nakajima, K., et al. 2017, *PASJ*, 69, 1
- Kojima, T., Ouchi, M., Rauch, M., et al. 2019, arXiv:1910.08559
- Komiyama, Y., Obuchi, Y., Nakaya, H., et al. 2018, *PASJ*, 70, 1
- Kroupa, P. 2001, *MNRAS*, 322, 231
- Kroupa, P., & Weidner, C. 2003, *ApJ*, 598, 1076
- Kunth, D., & Östlin, G. 2000, *A&A*, 10, 1
- Lecureur, A., Hill, V., Zoccali, M., et al. 2007, *A&A*, 465, 799
- Lehner, N., Howk, J. C., Tripp, T. M., et al. 2013, *ApJ*, 770, doi:10.1088/0004-637X/770/2/138
- López-Sánchez, A. R., & Esteban, C. 2009, *A&A*, 508, 615
- López-Sánchez, A. R., & Esteban, C. 2010, *A&A*, 516, A104
- Luridiana, V., Morisset, C., & Shaw, R. A. 2015, *A&A*, 573, A42
- Lusso, E., Comastri, A., Vignali, C., et al. 2010, *A&A*, 512, A34
- Ly, C., Malkan, M. A., Nagao, T., et al. 2014, *ApJ*, 780, 122
- Mainali, R., Kollmeier, J. A., Stark, D. P., et al. 2017, *ApJ*, 836, L14
- Martizzi, D., Vogelsberger, M., Artale, M. C., et al. 2019, *MNRAS*, 486, 3766
- Matsumoto, H., Tsuru, T. G., Koyama, K., et al. 2001, *ApJ*, 547, L25
- Miyazaki, S., Komiyama, Y., Nakaya, H., et al. 2012, in *Proc. SPIE*, ed. I. S. McLean, S. K. Ramsay, & H. Takami, 84460Z
- Miyazaki, S., Komiyama, Y., Kawanomoto, S., et al. 2018, *PASJ*, 70, 1
- Nakajima, K., Ellis, R. S., Iwata, I., et al. 2016, *ApJ*, 831, L9
- Nakajima, K., & Ouchi, M. 2014, *MNRAS*, 442, 900
- Nomoto, K., Kobayashi, C., & Tominaga, N. 2013, *ARA&A*, 51, 457
- Ohkubo, T., Umeda, H., Maeda, K., et al. 2006, *ApJ*, 645, 1352
- Oke, J. B., & Gunn, J. E. 1983, *ApJ*, 266, 713
- Omukai, K., & Palla, F. 2003, *ApJ*, 589, 677
- Ono, Y., Ouchi, M., Harikane, Y., et al. 2018, *PASJ*, 70, 2
- Pérez-Montero, E., & Contini, T. 2009, *MNRAS*, 398, 949
- Pérez-Montero, E., Contini, T., Lamareille, F., et al. 2013, *A&A*, 549, A25
- Portegies Zwart, S. F., Baumgardt, H., Hut, P., Makino, J., & McMillan, S. L. 2004, *Nature*, 428, 724
- Portegies Zwart, S. F., Baumgardt, H., McMillan, S. L. W., et al. 2006, *ApJ*, 641, 319
- Portegies Zwart, S. F., Makino, J., McMillan, S. L., & Hut, P. 1999, *A&A*, 348, 117
- Press, W. H., Teukolsky, S. A., Vetterling, T. W., & Flannery, B. P. 2007, *Numerical Recipes, The Art of Scientific Computing* (Cambridge University Press)
- Prochaska, J. X., Gawiser, E., Wolfe, A. M., Castro, S., & Djorgovski, S. G. 2003, *ApJ*, 595, L9
- Quiret, S., Péroux, C., Zafar, T., et al. 2016, *MNRAS*, 458, 4074
- Rafelski, M., Wolfe, A. M., Prochaska, J. X., Neeleman, M., & Mendez, A. J. 2012, *ApJ*, 755, 89
- Rodriguez, M., & Rubin, R. H. 2005, *ApJ*, 626, 900
- Santoro, F., & Shull, J. M. 2006, *ApJ*, 643, 26
- Schaerer, D., Fragos, T., & Izotov, Y. I. 2019, *A&A*, 622, L10
- Schlegel, D. J., Finkbeiner, D. P., & Davis, M. 1998, *ApJ*, 500, 525
- Schneider, R., Omukai, K., Inoue, A. K., & Ferrara, A. 2006, *MNRAS*, 369, 1437
- Senchyna, P., Stark, D. P., Vidal-García, A., et al. 2017, *MNRAS*, 472, 2608
- Shirazi, M., & Brinchmann, J. 2012, *MNRAS*, 421, 1043
- Skillman, E. D. 1989, *ApJ*, 347, 883
- Smith, B. D., & Sigurdsson, S. 2007, *ApJ*, 661, L5
- Stanway, E. R., Eldridge, J. J., & Becker, G. D. 2016, *MNRAS*, 456, 485
- Stark, D. P., Richard, J., Siana, B., et al. 2014, *MNRAS*, 445, 3200
- Stark, D. P., Walth, G., Charlot, S., et al. 2015, *MNRAS*, 454, 1393
- Stasińska, G., & Izotov, Y. 2003, *A&A*, 397, 71
- Stasińska, G., Izotov, Y., Morisset, C., & Guseva, N. 2015, *A&A*, 576, A83
- Steidel, C. C., Strom, A. L., Pettini, M., et al. 2016, *ApJ*, 826, 159
- Suzuki, A., & Maeda, K. 2018, *ApJ*, 852, 101
- Thuan, T. X., Lecavelier des Etangs, A., & Izotov, Y. I. 2005, *ApJ*, 621, 269
- Tominaga, N., Umeda, H., & Nomoto, K. 2007, *ApJ*, 660, 516
- Vanzella, E., Balestra, I., Gronke, M., et al. 2017, *MNRAS*, 465, 3803
- Vincenzo, F., Belfiore, F., Maiolino, R., Matteucci, F., & Ventura, P. 2016, *MNRAS*, 458, 3466
- Wise, J. H., Turk, M. J., Norman, M. L., & Abel, T. 2012, *ApJ*, 745, 50
- Xiao, L., Stanway, E. R., & Eldridge, J. J. 2018, *MNRAS*, 477, 904
- York, D. G., Adelman, J., Anderson, Jr., J. E., et al. 2000, *AJ*, 120, 1579
- Yungelson, L. R., Van Den Heuvel, E. P., Vink, J. S., Zwart, S. F., & De Koter, A. 2008, *A&A*, 477, 223